

Low Dynamic Range for RIS-aided Bistatic Integrated Sensing and Communication

Ahmad Bazzi and Marwa Chafii

Abstract—The following paper presents a reconfigurable intelligent surface (RIS)-aided integrated sensing and communication (ISAC) system model scenario, where a base station communicates with a user, and a bi-static sensing unit, i.e. the passive radar (PR), senses targets using downlink signals. Given that the RIS aids with communication and sensing tasks, this paper introduces new interfering paths that can overwhelm the PR with unnecessarily high power, namely the path interference (PI), which is itself a combination of two interfering paths, the direct path interference (DPI) and the reflected path interference (RPI). For this, we formulate an optimization framework that allows the system to carry on with its ISAC tasks, through analog space-time beamforming at the sensing unit, in collaboration with RIS phase shift and statistical transmit covariance matrix optimization, while minimizing the PI power. As the proposed optimization problem is non-convex, we tailor a block-cyclic coordinate descent (BCCD) method to decouple the non-convex sub-problem from the convex one. A Riemannian conjugate gradient method is devised to generate the RIS and PR space-time beamforming phase shifts per BCCD iteration, while the convex sub-problem is solved via off-the-shelf solvers. Simulation results demonstrate the effectiveness of the proposed solver when compared with benchmarking ones.

Index Terms—Integrated Sensing and Communication, ISAC, Reconfigurable Intelligent Surfaces, RIS, 6G

I. INTRODUCTION

Research in the realm of 6G anticipates future services and applications to address diverse market demands and disruptive technologies [1]. 6G's objectives include supporting a range of services such as blockchain, haptic telemedicine, VR/AR remote services, holographic teleportation, and extended reality (XR). This transcends conventional connectivity, incorporating sensing, computing, and leveraging environmental data for artificial intelligence and machine learning. However, bandwidth-intensive applications require a substantial capacity increase, expected to surge by a factor of 10^3 by 2030 [2]. Crucial roles are attributed to enabling technologies like sub-6 GHz, milli-meter wave (mmWave) frequencies, and reconfigurable intelligent surface (RIS). 6G is also anticipated to support integrated sensing and communication (ISAC) applications. Indeed, radar sensing and wireless communication share numerous similarities in signal processing and system design [3]. ISAC holds promise for groundbreaking applications, particularly in the automotive sector [4], the Internet of things, and robotics. ISAC collaboration and convergence are crucial features that can pave the way for innovations such as Vehicle-to-Everything (V2X) communication [5], leveraging high-rate

communications and high-precision localization capabilities. ISAC has been explored across various scenarios and challenges, including non-orthogonal multiple access (NOMA) [6], holographic communications [7], waveform design [8], security [9], and beamforming design [10].

RISs [11]–[15], comprised of adaptable reflecting elements, have garnered significant attention for their potential to enhance the capacity and coverage of wireless sensor networks [16]. These structures manipulate incident signals in the wireless propagation environment, thereby altering wireless channels between network nodes. RISs provide a low-energy consumption solution, enabling signal amplification without the need for power amplifiers. Their cost-effectiveness could lead to large-scale deployment, covering entire building walls [17]. The appropriately designed phase shifts from each reflecting element collectively combine reflected signals, commonly referred to as large intelligent surface/antennas (LISA) or intelligent reflecting surface (IRS) in the literature. RISs find applications in various wireless communication aspects, including beamforming, security, orthogonal frequency-division multiplexing (OFDM), and millimeter-wave channel estimation [18]–[20]. Their deployment enhances spectral and energy efficiency, supports environmentally friendly deployment, and contributes to secure wireless communication [21], [22]. On the other hand, passive radar (PR), a radar design that detection and localization of targets without emitting controlled radar data, has been extensively studied [23], [24]. Moreover, RIS is anticipated to play a pivotal role in advanced localization and sensing through PR. In addition, PR offers cost-effective procurement, operation, and maintenance, as well as covert operation. However, it encounters challenges in target detection due to the absence of transmitted waveform information. Nonetheless, it remains protocol-agnostic and operates without active component assistance.

To begin, forthcoming wireless networks designed to accommodate ISAC are anticipated to confront challenges related to paths undergoing single, double, and triple pathloss, particularly with the recent advancements in RIS. Despite these developments, little attention has been given to dynamic range considerations for ISAC, creating a significant gap in addressing this critical issue. Specifically, the dynamic range, representing the ratio between the highest and lowest power levels of signal components, determines the number of bits required by a receiver's analog-to-digital converter (ADC) to minimize quantization errors for accurate signal processing. However, simply increasing the number of bits results in greater power consumption. Hence, it is imperative to precisely identify the relevant signal components to economize the dynamic range efficiently.

Ahmad Bazzi and Marwa Chafii are with the Engineering Division, New York University (NYU) Abu Dhabi, 129188, UAE and NYU WIRELESS, NYU Tandon School of Engineering, Brooklyn, 11201, NY, USA (email: ahmad.bazzi@nyu.edu, marwa.chafii@nyu.edu).

Manuscript received xxx

It is important to note that there is ongoing research works on RIS [25] for ISAC systems to advance the road towards 6G [26]. The work in [27] designs RIS-aided ISAC beamforming for optimizing spectrum utilization via lightweight unsupervised learning-based methods that can achieve high spectrum efficiency. Also, [28] considers beamforming for RIS-ISAC systems to precode both communication symbols and radar waveforms. Additionally, [29] explores an RIS-assisted ISAC system where a multi-antenna base station (BS) handles both multi-user communications and radar sensing, focusing on optimizing target detection and parameter estimation. Two non-convex optimization problems are addressed to maximize the sum-rate under signal-to-noise ratio (SNR) and Cramér-Rao bound (CRB) constraints, with algorithms developed to solve the optimization problems. Furthermore, [30] presents an ISAC system utilizing RIS, with simultaneous beam training and target sensing that differentiates between RIS and target echoes, with low-complexity positioning and array orientation estimation methods to facilitate beam alignment. In addition, [31] derives sensing algorithms for joint angle of arrival (AoA) and time of arrival (ToA) estimation in a communication-centric RIS assisted bistatic scenario incorporating a PR. The work in [32] addresses the challenge of limited degrees-of-freedom (DoF) in ISAC systems by leveraging RIS to enhance beamforming capabilities. For this, two optimization techniques are proposed: an alternating optimization algorithm combining semidefinite relaxation and one-dimension iteration to maximize radar mutual information, and another to optimize weighted ISAC performance. In terms of co-existence, [33] proposes a double-RIS-assisted ISAC system to enhance communication signals and suppress mutual interference in communication-radar coexistence scenarios. More specifically, [33] introduces a penalty dual decomposition-based algorithm for joint beamforming optimization, addressing both high and low radar power cases. From a security perspective, [34] focuses on the security challenges arising in ISAC systems by optimizing a simultaneous transmitting and reflecting (STAR)-RIS [35] assisted setup, which maximizes the sum secrecy rate while ensuring the necessary beampattern gain for target sensing, through proper optimization techniques. In the context of STAR-RIS for ISAC, [36] studies a structured transmission structure for the ISAC schemes in high mobility scenarios.

The focus of this paper is on a situation where a PR is exposed to a signal-of-opportunity arising from communication signals transmitted by the BS, and further reflected off-targets, ultimately reaching the PR. As the bi-static configuration is widely utilized in radar applications, it presents a notable issue that could potentially elevate costs for future ISAC systems. The direct path interference (DPI) is a common problem within the bi-static radar literature [37], and its suppression is crucial for practical radar operations [37], [38]. With the introduction of RIS, the power imbalances stemming from single, double, and triple path-loss will overshadow the PR with unnecessary high-power differentials. This is primarily attributed to the BS→PR and BS→RIS→PR paths in contrast to other sensing paths involving the target. Analog domain suppression is one direction that can be employed to mitigate the DPI in bi-static and passive radar. Indeed, if we were lucky enough to

choose an ADC with infinite resolution, delegating part of this cancellation to analog would not be necessary. . So, analog domain processing, including analog beamforming, can help in reducing the dynamic range before digital conversion when low-cost, low-power, or low-resolution ADCs are integrated, so as not to degrade the received signal purity. Moreover, analog domain processing is simple as the components involved typically consist of couplers and phase compensators [39]; yet providing substantial suppression capabilities which can vary from 30 to 70 dB, depending on the implementation complexity [40]. In this context, a DPI suppression method was implemented in the analog domain before the digital conversion was proposed in [41] for frequency modulation (FM) based passive radars. Related suppression techniques may include methods such as null-steering and physical shielding, which are only moderately effective and can limit the system's feasibility [42]. In this paper, and inspired by the reasoning of delegating interference cancellation to the analog domain, we allow the PR to incorporate space-time beamforming, by adjusting phase shifts across space and time in order to pragmatically mitigate any potential interfering tasks, while allowing the PR to carry on its sensing task.

This work focuses on an ISAC system model in the presence of a receiving sensing unit, i.e. the PR and a RIS where the goal is to optimize for communication SNRs and radar signal-to-noise-and-distortion ratios (SNDRs) while maintaining a low path interference (PI) at the PR. To that purpose, we have summarized our contributions as follows.

- **RIS-aided ISAC system with PR.** We model a RIS-aided ISAC system model, where the BS along with the RIS can together help the PR, reduce the dynamic range due to high PI, in conjunction with analog beamforming at the PR, while performing ISAC tasks.
- **Figure of merit and motivation** We extend the definition of DPI, which is a known interference path in bistatic models, to the more general PI which arises due to the presence of a RIS in the scene. Essentially, the PI is the sum of the DPI and the reflected path interference (RPI), where the later is due to the BS→RIS→PR path. We then provide context as to why this figure-of-merit is important, and the reverberations it has on *flooding the sensing architecture with a non-reasonably high dynamic range*.
- **RIS-ISAC optimization framework.** We propose an optimization framework tailored for minimizing the resulting high dynamic range while maintaining given ISAC performance in terms of communication SNR, as well as radar SNDR. In particular, the BS optimizes its statistical covariance matrix, along with the RIS phase shifts and the PR analog phase shifts to jointly minimize the strong PI component, whilst maintaining given radar SNDR and communication SNRs levels.
- **Solution via block cyclic coordinate descent.** As the proposed RIS-ISAC optimization problem is non-convex and highly non-linear, we design a block cyclic coordinate descent (BCCD) algorithm that decomposes the problem into two sub-problems, one of which contains is

non-linear and non-convex, and solved via an Riemannian conjugate gradient (RCG) method, and the other is an semi-definite program (SDP), hence convex. The BCCD then iterates between the two problems and converges to a stable solution providing the statistical transmit covariance matrix, as well as the RIS phase shifts and PR analog phase shifts.

- **Computational Complexity Analysis.** We present an analysis of the computational complexity associated with the solutions of the proposed optimization problems for low dynamic range bistatic ISAC in terms of "big-oh" complexity.
- **Extensive simulation results.** We present extensive simulation results that highlight the superiority, as well as the potential of the proposed design and algorithm with respect to many benchmarks, in terms of achievable dynamic ranges, radar SNDR and communication SNR.

Moreover, we unveil some important insights, i.e.

- Increasing the number of transmit antennas effectively reduces the dynamic range required at PR, which was observed across all benchmarks and the proposed method. Specifically, in scenarios with high M_t , doubling the number of antennas tends to decrease the dynamic range by approximately 5 dB. Moreover, the quantity of antennas at the PR enhances analog beamforming capabilities, further reducing the dynamic range needed. For instance, transitioning from 1 to 16 antennas presents a near 10 dB dynamic range reduction, with an additional 10 dB decrease when quadrupling from 16 to 64 antennas using the proposed method. Remarkably, the proposed method achieves a dramatic reduction in dynamic range by up to 50 dB compared to setups without a RIS, highlighting the method's efficiency in integrating PI management directly into the optimization process.
- The proposed method reveals a significant advantage in achieving high communication SNR at substantially lower dynamic ranges compared to benchmark methods, indicating its efficiency in optimizing system performance with limited dynamic range. For instance, to achieve a communication SNR of 30 dB, the proposed approach requires only a 23 dB dynamic range with only a single antenna at the PR, whereas benchmarks necessitate over 100 dB. Secondly, a counter-intuitive observation emerges where increasing the number of antennas M allows for enhanced communication SNR at a fixed dynamic range. For example, a dynamic range of 20 dB achieves a 26 dB communication SNR with one antenna but can reach 35 dB SNR with 16 antennas and exceed 40 dB with 64 antennas.
- We observe that prioritizing communication tasks over sensing tasks can significantly reduce the PI power level for fixed resources (i.e. RIS size and antennas at the PR). Specifically, simulations reveal that increasing the communication priority leads to a marked decrease in PI power levels, particularly with the proposed method demonstrating the most substantial reduction, highlighting the effectiveness of communication prioritization in

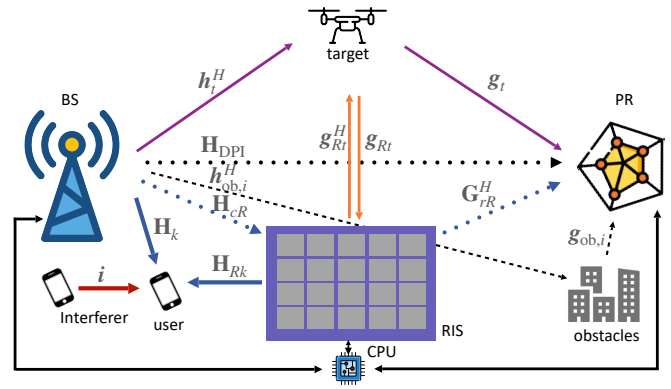


Fig. 1. The RIS-aided bistatic ISAC system. Two paths are contributing to the PI at PR, namely the DPI (i.e. the direct one) and the RPI due to BS→RIS→PR. Four paths arise due to the target's presence, namely the BS→target→PR path, the BS→target→RIS→PR path, the BS→RIS→target→PR path, and the BS→RIS→target→RIS→PR path. Two more paths are seen at the user, i.e. the BS→user direct path and the BS→RIS→user path. There are also possible interferers and obstacles within the scene.

mitigating PI in RIS-ISAC systems.

The following paper is organized as follows: Section II presents the ISAC system model for the underlying problem in the presence of a RIS. Section III describes the main motivation, in addition to the importance of addressing dynamic range in our ISAC RIS-aided problem. Moreover, Section IV formulates an ISAC optimization problem aiming at optimizing the dynamic range at the sensing unit, i.e. the PR. In addition, we introduce an efficient solver to tackle the non-convex problem at hand. Section V presents our simulation results. Section VI discusses open challenges for future RIS-aided ISAC bi-static systems. Section VII concludes the paper.

Notation: Upper-case and lower-case boldface letters denote matrices and vectors, respectively. $(\cdot)^T$, $(\cdot)^*$ and $(\cdot)^H$ represent the transpose, the conjugate and the transpose-conjugate operators. The set of all complex-valued $N \times M$ matrices is $\mathbb{C}^{N \times M}$. The trace is $\text{tr}(\cdot)$. The $N \times N$ identity matrix is \mathbf{I}_N . We index the $(i, j)^{th}$ element of \mathbf{A} as $\mathbf{A}(i, j)$. The Kronecker product is \otimes . The Hadamard product is \odot . The $\text{diag}(\cdot)$ operator applied onto a vector \mathbf{x} , i.e. $\text{diag}(\mathbf{x})$ returns a diagonal matrix consisting of entries of \mathbf{x} . $[\mathbf{x}]_m$ returns the m^{th} element of vector \mathbf{x} . The statement $\mathbf{A} \succeq \mathbf{B}$ means that $\mathbf{A} - \mathbf{B}$ is a positive semi-definite matrix. All other notations are defined within the manuscript's text.

II. SYSTEM MODEL

Consider an ISAC system comprised of a target of interest, a multi-antenna communication user, and a communication BS, an RIS, and a PR. The BS is equipped with an antenna array composed of M_t elements, whereas the communication user is equipped with M_r antennas. Also, assume that a RIS containing N reflecting elements is present. In addition, the PR senses the channel through M receive antennas, without any probing signal for transmission. Fig. 1 depicts a BS broadcasting the same signal vector to communication users and an intended target of interest. Communication users are considered to be located at random positions. In what follows, we present the signal models for the communication and sensing systems. We note that perfect channel state information (CSI) is assumed

for all channels.

A. Communication Model

Denote $\mathbf{S} = [\mathbf{s}_1, \mathbf{s}_2, \dots, \mathbf{s}_{M_t}]^\top \in \mathbb{C}^{M_t \times L}$ by the transmit waveform matrix of the communication system transmitted by the BS, where \mathbf{s}_m represents the transmit signal of the m^{th} antenna element of the BS, $\forall m = 1, 2, \dots, M_t$. In addition, L denotes the number of time samples transmitted by the BS. To this end, the received communication signals can be written as

$$\mathbf{Y}_c = (\gamma_d^c \mathbf{H}_k + \gamma_r^c \mathbf{H}_{\text{Rk}} \Phi \mathbf{H}_{\text{cR}}) \mathbf{S} + \mathbf{H}_I \mathbf{S}_I + \mathbf{N}_c, \quad (1)$$

where $\mathbf{H}_k \in \mathbb{C}^{M_r \times M_t}$ and $\mathbf{H}_{\text{Rk}} \in \mathbb{C}^{M_r \times N}$ are the normalized channel responses (the small-scale channel matrix) from the BS to the user, and from the RIS to the user, respectively. Moreover, $\mathbf{H}_{\text{cR}} \in \mathbb{C}^{N \times M_t}$ represents the normalized channel response from the BS to the RIS. In addition, $\Phi = \text{diag}(\phi)$ is the reflection matrix of the RIS, whereby $\phi = [\phi_1, \dots, \phi_N]^\top$ is the vector of reflecting coefficients, and $|\phi_n| = 1, \forall n = 1, \dots, N$. In addition, the matrix $\mathbf{S}_I \in \mathbb{C}^{M_r \times L}$ is an interference matrix arising from various sources, such as co-channel interference. Also \mathbf{H}_I is the interferer's channel. The direct and reflected complex channel gains are denoted as $\gamma_d^c \in \mathbb{C}$ and $\gamma_r^c \in \mathbb{C}$, respectively, which follow the single and double pathloss equations [43], [44] namely

$$|\gamma_d^c| = \sqrt{\frac{\lambda^2 P_T G_T G_R^c}{(4\pi)^2 d_k^2}}, \quad |\gamma_r^c| = \sqrt{\frac{\lambda^2 P_T G_T G_R^c \sigma_{\text{RIS}}}{(4\pi)^3 d_{\text{Rk}}^2 d_{\text{cR}}^2}}. \quad (2)$$

The transmit power by the BS is denoted as P_T , the BS's transmit antenna gain is G_T and the user's receive antenna gain is G_R^c . The distances d_k , d_{Rk} , and d_{cR} represent the distance between the BS and the user, between the BS and the RIS and between the RIS and user, respectively. $\lambda = \frac{c}{f_c}$ is the wavelength, where the carrier frequency is f_c and c is the speed of light. In the far-field region, the radar cross-section (RCS) of each RIS element is as follows [45]

$$\sigma_{\text{RIS}} = \frac{4\pi A^2 S_{\text{sub}}^2}{\lambda^2} F(\varphi_r, \vartheta_r) F(\varphi_t, \vartheta_t), \quad (3)$$

where A is the reflecting coefficient of the RIS element, which is 1 in case of passive RIS. Moreover, $S_{\text{sub}} = d_x \times d_y$ represents the area of each RIS element. d_x and d_y stand for the size of the RIS along the x and y dimensions, respectively. Also, (φ^r, ϑ^r) and (φ^t, ϑ^t) denote the azimuth and elevation angles pointing from the center of the RIS to the BS and target/PR. In addition, $F(\varphi_r, \vartheta_r)$ and $F(\varphi_t, \vartheta_t)$ denote the normalized power radiation patterns of the RIS element in the directions of reflecting and receiving. The reflecting coefficient of the RIS elements is $A = 1$ for passive RIS.

Finally, in compact notation, we can write the signal model in equation (4) in vectorized form as

$$\mathbf{y}_c = \mathbf{H}_c(\phi) \mathbf{s} + \bar{\mathbf{H}}_I \mathbf{s}_I + \mathbf{n}_c, \quad (4)$$

where $\mathbf{y}_c = \text{vec}(\mathbf{Y}_c)$, $\mathbf{n}_c = \text{vec}(\mathbf{N}_c)$, $\mathbf{s} = \text{vec}(\mathbf{S})$ and $\mathbf{s}_I = \text{vec}(\mathbf{S}_I)$ and

$$\mathbf{H}_c(\phi) = \mathbf{I}_L \otimes (\gamma_d^c \mathbf{H}_k + \gamma_r^c \mathbf{H}_{\text{Rk}} \Phi \mathbf{H}_{\text{cR}}). \quad (5)$$

A similar definition can be made on $\bar{\mathbf{H}}_I$. It is worth noting that the communication channels \mathbf{H}_k , \mathbf{H}_{Rk} , \mathbf{H}_{cR} include line-of-sight (LoS) and non-line-of-sight (NLoS) components that may arise within the wireless propagation. In particular, \mathbf{H}_k

contains multipath components between the BS and the communication user, \mathbf{H}_{Rk} may also accommodate any possible static/dynamic obstacles arising between the communication user and the RIS, and \mathbf{H}_{cR} can contain obstacles between the BS and the RIS.

For the sake of tractability of the analysis below, we shall consider that the interference vector \mathbf{s}_I is Gaussian distributed with variance equal to average interference power, say σ_I^2 . This assumption is indeed a "worst case scenario", since, for communications, Gaussian distribution injected onto the signal of interest, yields worst case capacity [46], [47]. As a result of this assumption, we model $\bar{\mathbf{H}}_I \mathbf{s}_I$ as an additive white Gaussian noise (AWGN) zero-mean and variance σ_I^2 , which represents the average noise power at the user due to interference. Meanwhile, \mathbf{n}_c is also modeled as zero-mean and variance σ_n^2 . This means that the quantity $\bar{\mathbf{H}}_I \mathbf{s}_I + \mathbf{n}_c$ is itself zero-mean AWGN with variance $\sigma_c^2 = \sigma_I^2 + \sigma_n^2$, i.e. the worst case interference can be viewed as added AWGN.

B. Sensing Model

Referring to Fig. 1, we can see that the signal at the PR arrives from multiple sources. The first components we model are referred to as PI, which include two main components, comprising two primary elements: the DPI and the RPI. As the name suggests, the DPI arises due to the direct channel between the BS and PR. Denoting $\mathbf{H}_{\text{DPI}} \in \mathbb{C}^{M \times M_t}$ as the normalized DPI channel response and $\mathbf{H}_{\text{RPI}} \in \mathbb{C}^{M \times M_t}$ as the normalized RPI channel response, we can formally define the PI channel as

$$\mathbf{H}_{\text{PI}} = \gamma_{\text{DPI}} \mathbf{H}_{\text{DPI}} + \gamma_{\text{RPI}} \mathbf{H}_{\text{RPI}}, \quad (6)$$

where

$$\mathbf{H}_{\text{RPI}} = \mathbf{G}_{\text{rR}}^H \Phi \mathbf{H}_{\text{cR}}, \quad (7)$$

and $\mathbf{G}_{\text{rR}} \in \mathbb{C}^{N \times M}$ represents the normalized channel response from the PR to the RIS. Similar to (2), $\gamma_{\text{DPI}} \in \mathbb{C}$ and $\gamma_{\text{RPI}} \in \mathbb{C}$ denote the complex channel gains of the DPI and RPI, respectively, and are given as follows

$$|\gamma_{\text{DPI}}| = \sqrt{\frac{\lambda^2 P_T G_T G_R^{\text{PR}}}{(4\pi)^2 d_{\text{DPI}}^2}}, \quad |\gamma_{\text{RPI}}| = \sqrt{\frac{\lambda^2 P_T G_T G_R^{\text{PR}} \sigma_{\text{RIS}}}{(4\pi)^3 d_{\text{rR}}^2 d_{\text{cR}}^2}},$$

where all quantities are already defined except for G_R^{PR} which is the antenna gain at the PR and d_{rR} which is the distance between the RIS and PR. For a detailed motivation on the importance of mitigating the PI, especially in practical scenarios with limited dynamic range, the reader is referred to Section III.

Furthermore, Fig. 1 illustrates that the useful sensing signal to sense the target from PR's perspective can be modeled through four paths: (i) In the first path, i.e. BS \rightarrow target \rightarrow PR, the transmit waveforms hit the target and then echoes back to the PR. This channel is denoted as $\gamma_1^s \mathbf{g}_t \mathbf{h}_t^H$, whereby $\mathbf{g}_t \in \mathbb{C}^{M \times 1}$ denotes the target response associated with the direct channel between the target and PR and $\mathbf{h}_t \in \mathbb{C}^{M_t \times 1}$ models the channel between the BS and the target. Also, $\gamma_1^s \in \mathbb{C}$ is the complex channel gain due to the first path, and follows a double pathloss equation similar to γ_r^c in equation (1), but with the exception of σ_t to account for the bistatic RCS of the target. (ii) In the second path, which

is BS \rightarrow target \rightarrow RIS \rightarrow PR, the transmit signal reaches the target and then backscatters to the PR via RIS. This channel can be written as $\gamma_2^s \mathbf{G}_{\text{rR}}^H \Phi \mathbf{g}_{\text{Rt}} \mathbf{h}_t^H$, where $\mathbf{g}_{\text{Rt}} \in \mathbb{C}^{N \times 1}$ represents the normalized channel between the target and the RIS. Furthermore, $\gamma_2^s \in \mathbb{C}$ is the complex channel gain due to the second path and follows a triple pathloss equation. (iii) The third path, namely BS \rightarrow RIS \rightarrow target \rightarrow PR, captures the transmit waveforms which hits the RIS first. This channel can be expressed as $\gamma_3^s \mathbf{g}_t \mathbf{g}_{\text{Rt}}^H \Phi \mathbf{H}_{\text{cR}}$. In addition, $\gamma_3^s \in \mathbb{C}$ is the complex channel gain due to the third path also is in accordance of a triple pathloss equation. Finally, (iv) the fourth path, which is BS \rightarrow RIS \rightarrow target \rightarrow RIS \rightarrow PR, the transmit waveforms propagates first towards the PR, similar to the third path, but then it is reflected toward the target, and backscattered to the radar receivers. This channel can be expressed as $\gamma_4^s (\mathbf{G}_{\text{rR}}^H \Phi \mathbf{g}_{\text{Rt}}) (\mathbf{g}_{\text{Rt}}^H \Phi \mathbf{H}_{\text{cR}})$. Moreover, $\gamma_4^s \in \mathbb{C}$ is the complex channel gain arising due to the fourth path and abides by a quadruple pathloss equation. For a detailed explanation on the *four-path model*, the reader is referred to [48], [49]. To this end, the signal received at the PR can be written as

$$\mathbf{Y}_t = \mathbf{H}_{\text{PI}} \mathbf{S} + (\gamma_1^s \mathbf{g}_t \mathbf{h}_t^H + \gamma_2^s \mathbf{G}_{\text{rR}}^H \Phi \mathbf{g}_{\text{Rt}} \mathbf{h}_t^H + \gamma_3^s \mathbf{g}_t \mathbf{g}_{\text{Rt}}^H \Phi \mathbf{H}_{\text{cR}} + \gamma_4^s \mathbf{G}_{\text{rR}}^H \Phi \mathbf{g}_{\text{Rt}} \mathbf{g}_{\text{Rt}}^H \Phi \mathbf{H}_{\text{cR}}) \mathbf{S} + \sum_{i=1}^Q \gamma_i^{\text{ob}} \mathbf{g}_{\text{ob},i} \mathbf{h}_{\text{ob},i}^H \mathbf{S} + \mathbf{N}_r, \quad (8)$$

where the first term arises due to the PIs. Moreover, the second term factors the four sensing paths. The third term, i.e. $\sum_{i=1}^Q \gamma_i^{\text{ob}} \mathbf{g}_{\text{ob},i} \mathbf{h}_{\text{ob},i}^H \mathbf{S}$ defines the possible ever-changing obstacles found in the scene, e.g. moving clutter [50]. More specifically, γ_i^{ob} is the complex channel gain arising from the i^{th} obstacle, including its RCS and possible doppler shift in the dynamic case. Moreover, $\mathbf{g}_{\text{ob},i} \in \mathbb{C}^{M \times 1}$ is the response associated with the direct channel between the i^{th} obstacle and PR and $\mathbf{h}_{\text{ob},i} \in \mathbb{C}^{M_t \times 1}$ models the channel between the i^{th} obstacle and the BS. In addition, Q represents the number of obstacles in the scene. The last term, i.e. \mathbf{N}_r represents the PR background noise.

In a very compact way, and similar to (4), we vectorize the received signal at the PR in (8) as

$$\mathbf{y}_t = \mathbf{A}_c(\phi) \mathbf{s} + \mathbf{A}_r(\phi) \mathbf{s} + \mathbf{A}_o(\phi) \mathbf{s} + \mathbf{n}_r, \quad (9)$$

where $\mathbf{y}_t = \text{vec}(\mathbf{Y}_t)$, $\mathbf{n}_r = \text{vec}(\mathbf{N}_r)$ and

$$\mathbf{A}_c(\phi) = \mathbf{I}_L \otimes \mathbf{H}_{\text{PI}}, \quad (10)$$

and

$$\mathbf{A}_r(\phi) = \mathbf{I}_L \otimes (\gamma_1^s \mathbf{g}_t \mathbf{h}_t^H + \gamma_2^s \mathbf{G}_{\text{rR}}^H \Phi \mathbf{g}_{\text{Rt}} \mathbf{h}_t^H + \gamma_3^s \mathbf{g}_t \mathbf{g}_{\text{Rt}}^H \Phi \mathbf{H}_{\text{cR}} + \gamma_4^s \mathbf{G}_{\text{rR}}^H \Phi \mathbf{g}_{\text{Rt}} \mathbf{g}_{\text{Rt}}^H \Phi \mathbf{H}_{\text{cR}}). \quad (11)$$

Furthermore, we have that

$$\mathbf{A}_o(\phi) = \mathbf{I}_L \otimes \sum_{i=1}^Q \gamma_i^{\text{ob}} \mathbf{g}_{\text{ob},i} \mathbf{h}_{\text{ob},i}^H. \quad (12)$$

In the following section, we highlight the importance of mitigating components arising from PIs for ISAC applications.

C. ISAC Central Processing

A central processing unit (CPU) could be incorporated to perform the processing, as depicted in Fig. 1. At an initial phase, the CPU can generate the statistical transmit

covariance matrix towards the BS, the RIS phase shifts, and the space-time analog beamformer to the PR through back-hauling capacity links, after solving the optimization problems discussed in the coming sections. These quantities can then be communicated back to the BS, RIS, and PR, allowing them to make the necessary adjustments. In the subsequent phase, the BS would transmit its data symbols via the obtained covariance matrix, whereas the PR performs space-time beamforming for the target detection process. If a target exists, then the received signal is forwarded back to the CPU for further sensing analysis, e.g. delay-Doppler processing, i.e. a range-Doppler map is formed [51], to estimate the range and speed of the target.

III. MOTIVATION & IMPORTANCE OF DYNAMIC RANGE

The majority of existing designs neglect the limited dynamic range of practical receivers. Formally speaking, the *dynamic range* describes the range of the input signal levels that can be reliably measured at the same time. Said differently, it is the capability to sense small signals in the presence of dominating ones [52]. This issue becomes more pronounced in ISAC applications with RIS integrations, as strong signals can "flood" the ADC with un-necessary power. Indeed, the analog radio frequency (RF) architecture at the PR must be able to ensure proper reception of the weak reflected signals, given the high direct paths total power. To highlight this, the self-interference caused by the BS onto the PR, which is referred to in radar literature as DPI (also known as "direct signal interference" [53]), is most likely multiple orders of magnitude higher than the desired receive signal conveying informative sensing information. Putting it in context, the power level gap between these components can exceed 100 dB, as noted in [54]. This, in turn, can overwhelm and saturate components of the PR's receive chain if not pragmatically mitigated. In a traditional bi-static scenario, the dynamic range is determined by the ratio of the DPI power to the thermal noise level, given that the interest lies in achieving sensitivity down to noise level [55]. This arises because, when considering a single target and neglecting clutter, the transmission between transmit and receive units in a bi-static setup can be modeled by only two paths: the DPI and the direct echo (DE), as illustrated in Fig. 2a. In contrast, when a RIS is present, we can distinguish between four main paths as shown in Fig. 2b, two of which are shared with the traditional bi-static scenario (i.e. the DPI and DE) and two others naturally appearing due to the presence of the RIS, namely the RPI and the RIS-resulted echo (RE). It follows that the dynamic range will not only be determined by the DPI power, but also by the RPI one, which can also be orders of magnitude stronger than the DE and RE. Following [55], we can then say that the ADC's dynamic range at the PR must satisfy the following condition in order to obtain sensitivity at the level of the thermal noise, i.e. in order to accommodate the PI component at a given noise floor

$$\text{DR} \geq \frac{P_{\text{PI}}}{P_{\text{noise}}}, \quad (13)$$

where P_{PI} represents the total power of the "more general" PI with the useful echo signals, i.e. $P_{\text{PI}} = P_{\text{DPI}} + P_{\text{RPI}}$ where P_{DPI} and P_{RPI} are the powers of the DPI and RPI paths, respectively. Moreover, P_{noise} is thermal noise power

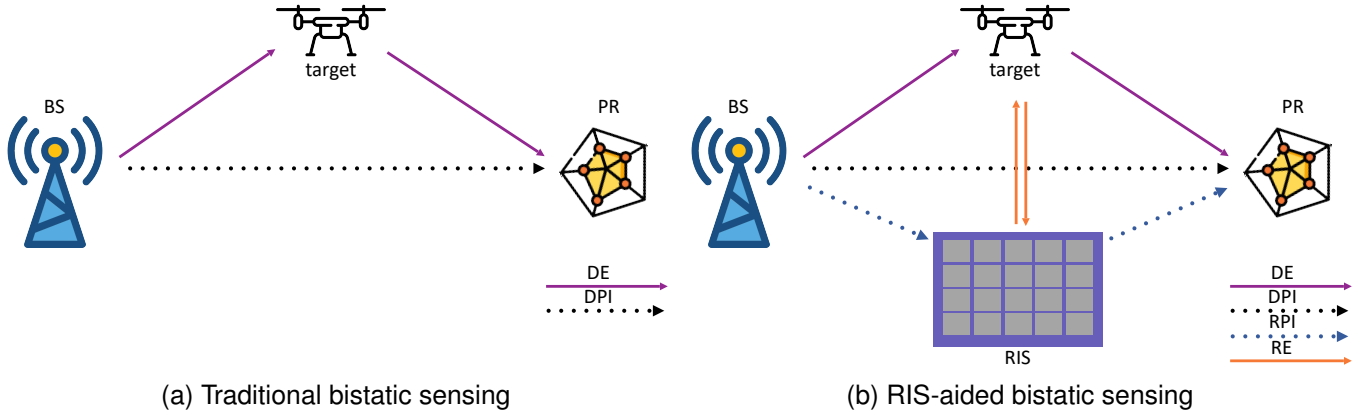


Fig. 2. Fundamental difference in PIs between the traditional and the RIS-aided bistatic settings. The setting in (a) contains only a DPI, as opposed to DPI-plus-RPI in (b).

which exists in all electronic devices operating at temperatures above absolute zero. It is expressed as $P_{\text{noise}} = k_B T_0 B_r$ [56], [57] where k_B is the Boltzmann constant, T_0 is the effective noise temperature at the PR, and B is the bandwidth of the PR. A common approach of dealing with DPI mitigation (or in this case, the PI) is through analog suppression [53], [58], [59], which could cancel certain portions of the DPI power. The main reason of this delegation is because the cancellation performance in the digital domain is limited by the dynamic range of the ADC at the PR. Of course, if we were fortunate enough to select an ADC with infinite resolution, there would be no need to allocate part of this suppression to the analog domain. Nevertheless, the dynamic range of currently available ADCs is insufficient to capture the power difference between the PI and all pertinent echoes, resulting in the loss of the desired received signal during the quantization process. Therefore, jointly reducing the powers of DPI and RPI can significantly reduce the dynamic range subsequently required by an embedded ADC within the receive path of the PR. The ADC's dynamic range is also a measure of the maximum SNR [60] by the ADC [61], which can be computed by the following formula [62], [63]

$$\text{SNR} = 6.02N_{\text{ENOB}} + 1.76 \text{ dBFS}, \quad (14)$$

where N_{ENOB} is the *effective number of bits* in the ADC resolution. For practicality reasons, it should be noted that the effective number of bits is the number of bits required by non-ideal ADCs, such as the sigma-delta ADC [64], to achieve the same effective resolution as an ideal ADC sampling at a resolution of N_{ENOB} [62]. In fact, the effective number of bits is upper bounded by the actual number of bits of an ADC, as the former contains further non-idealities [65], such as clipping, jitter and non-linearities. One example is the 14-bit AD 9683 [66] targeting communication applications, but an effective number of bits of around 11bits. Keep in mind that the quantizer is the main contributor to power consumption in an ADC. Consequently, having more bits per measurement directly leads to slower sampling rates and more expensive ADC costs [67]. Technically speaking, the dissipated ADC power is given as $P_{\text{ADC}} = \frac{2^b f_{\text{samp}}}{F}$, where b is the number

of bits used by the ADC's quantizer, f_{samp} is the ADC's sampling rate, and F is the figure of merit [68]. Hence, increasing b exponentially increases the required ADC power [69], [70]. Therefore, suppression of the PI prior to any PR signal processing or detection scheme is crucial for optimizing the effective number of bits, in order to improve radar detection capabilities and enhance the overall performance of the system.

IV. RIS-ISAC OPTIMIZATION WITH REDUCED DYNAMIC RANGE

A. Problem Statement

Assuming the PR is equipped with a space-time analog beamformer, i.e. $\mathbf{w} = [w_1 \dots w_{LM}]^T \in \mathbb{C}^{LM \times 1}$. More precisely, the space-time analog beamformer \mathbf{w} is applied before ADC conversion. Using the system model in equation (9), we can decompose the powers as follows

$$P_{\text{aBFin}} = \mathbb{E}(|\mathbf{w}^H \mathbf{y}_t|^2) = P_{\text{PI}} + P_{\text{sense}} + P_{\text{obs}} + P_{\text{noise}}, \quad (15)$$

where P_{PI} is the power of the PI over the observation time, P_{sense} is the power of the signal part containing useful sensing information at the PR, and P_{obs} represents the power due to reflections from obstacles over the observation time. Also, P_{noise} is the power of the noise at the PR. The power quantities can be verified to be

$$P_{\text{PI}} = \mathbf{w}^H \mathbf{A}_c(\phi) \mathbf{R}_{ss} \mathbf{A}_c^H(\phi) \mathbf{w}, \quad (16)$$

$$P_{\text{sense}} = \mathbf{w}^H \mathbf{A}_r(\phi) \mathbf{R}_{ss} \mathbf{A}_r^H(\phi) \mathbf{w}, \quad (17)$$

$$P_{\text{obs}} = \mathbf{w}^H \mathbf{A}_o(\phi) \mathbf{R}_{ss} \mathbf{A}_o^H(\phi) \mathbf{w}, \quad (18)$$

$$P_{\text{noise}} = \sigma_r^2 \|\mathbf{w}\|^2. \quad (19)$$

where $\mathbf{R}_{ss} = \mathbb{E}(\mathbf{s}\mathbf{s}^H)$ is the statistical covariance matrix of the transmit symbols \mathbf{s} . At this point, the PR's key performance indicator (KPI) can be defined through the SNDR (which can also be interpreted as a signal to interference plus noise ratio (SINR) [53]), which is given by [53](c.f. eqn. (10))

$$\text{SNDR} = \frac{P_{\text{sense}}}{P_{\text{PI}} + P_{\text{obs}} + P_{\text{noise}}}. \quad (20)$$

Note that the PI has been accommodated as part of interference at the PR, as some PI can still be found in the signal model even after suppression (namely the residual component). A remark here is that, compared to [53](c.f. eqn. (10)), we have

accounted for possible obstacles that can arise as interferers within the sensing SNDR. Now that all quantities are defined, we can clearly formulate our collaborative BS, RIS and PR optimization problem as follows

$$(\mathcal{P}) \left\{ \begin{array}{l} \min_{\mathbf{w}, \mathbf{R}_{ss}, \phi} P_{\text{PI}} \\ \text{s.t.} \quad \frac{\text{tr}(\mathbf{R}_{ss} \mathbf{H}_c^H(\phi) \mathbf{H}_c(\phi))}{M_r L \sigma_c^2} \geq \gamma_{\text{comm}}, \\ \frac{P_{\text{sense}}}{P_{\text{PI}} + P_{\text{obs}} + P_{\text{noise}}} \geq \gamma_{\text{sense}}, \\ |\phi_n| = 1, \quad n = 1 \cdots N, \\ |w_k| = 1, \quad k = 1 \cdots LM, \\ \text{tr}(\mathbf{R}_{ss}) = P_B, \quad \mathbf{R}_{ss} \succeq \mathbf{0}. \end{array} \right. \quad (21)$$

The proposed problem (\mathcal{P}) aims at minimizing the total PI power with only analog space-time processing at the level of the PR and RIS (namely through \mathbf{w} and ϕ configuration) and digital processing at the level of the BS, i.e. via \mathbf{R}_{ss} optimization. Moreover, the first constraint is the communication SNR, whereby γ_{comm} is the desired communication SNR to satisfy, which is given as input to the problem. Likewise, the second constraint guarantees a certain radar SNDR, where γ_{sense} is the minimum accepted target radar SNDR to guarantee. Note that the radar SNR (in this case radar SNDR) is a widely spread metric [71], [72]. The third and fourth constraints ensure constant-modulus solutions onto the RIS phase shifts and the analog space-time beamformer, respectively. The last constraint imposes a power constraint, where P_B is the available power budget. In addition, the last constraint imposes a positive definite constraint on the statistical covariance matrix of the transmit symbols. The problem (\mathcal{P}) is non-convex and difficult to solve in its current form. The non-convexity arises due to the constant-modulus constraints [73]. In the following subsection, we devise a BCCD tailored specifically for problem (\mathcal{P}) in (21).

B. Optimization via Block Cyclic Coordinate Descent Design

First, we solve a subproblem of equation (21), which is

$$(\mathcal{P}) \left\{ \begin{array}{l} \min_{\mathbf{w}, \phi} P_{\text{PI}} \\ \text{s.t.} \quad |\phi_n| = 1, \quad n = 1 \cdots N, \\ |w_k| = 1, \quad k = 1 \cdots LM. \end{array} \right. \quad (22)$$

Note that the above requires knowledge, or at least an estimate, of \mathbf{R}_{ss} . In the first iteration, a random initializer of \mathbf{R}_{ss} suffices. Before we proceed, we re-write the objective function P_{PI} , which gives us the following equivalent optimization problem

$$(\mathcal{P}_1) \left\{ \begin{array}{l} \min_{\mathbf{w}, \phi} \sum_{i=1}^{LM_t} |\mathbf{w}^H \mathbf{b}_i + \mathbf{w}^H \mathbf{C}_i \phi|^2 \\ \text{s.t.} \quad |\phi_n| = 1, \quad n = 1 \cdots N, \\ |w_k| = 1, \quad k = 1 \cdots LM. \end{array} \right. \quad (23)$$

where

$$\mathbf{b}_i = \sqrt{\lambda_i} \gamma_{\text{DPI}} (\mathbf{I}_L \otimes \mathbf{H}_{\text{DPI}}) \mathbf{v}_i \quad (24)$$

$$\mathbf{C}_i = \sqrt{\lambda_i} \gamma_{\text{RPI}} \mathbf{G}_{\text{rR}}^H \left[\text{diag}(\mathbf{H}_{\text{cR}} \mathbf{v}_i^{(1)}) \cdots \text{diag}(\mathbf{H}_{\text{cR}} \mathbf{v}_i^{(L)}) \right], \quad (25)$$

where $\mathbf{v}_i = \left[(\mathbf{v}_i^{(1)})^T \cdots (\mathbf{v}_i^{(L)})^T \right]^T$ and $\mathbf{v}_i^{(\ell)} \in \mathbb{C}^{M_t \times 1}$ for $\ell = 1 \cdots L$. The details are found in **Appendix A**. As the problem in (\mathcal{P}_1) is still non-convex, it is easier to tackle than the original problem in (\mathcal{P}) , which can be solved through an RCG algorithm. Before we proceed, we unify the variables into one variable $\mathbf{x} = [\mathbf{w}^T \ \phi^T]^T = [x_1 \cdots x_{N+LM}]^T$, hence we can easily re-write the problem as

$$(\mathcal{P}_1) \left\{ \begin{array}{l} \min_{\mathbf{w}, \phi} \sum_{i=1}^{LM_t} |\mathbf{x}^H \bar{\mathbf{b}}_i + \mathbf{x}^H \mathbf{D}_i \mathbf{x}|^2 \\ \text{s.t.} \quad |x_j| = 1, \quad j = 1 \cdots N + LM, \end{array} \right. \quad (26)$$

where $\bar{\mathbf{b}}_i$ is a zero-padded version of \mathbf{b}_i as follows $\bar{\mathbf{b}}_i = \left[\bar{\mathbf{b}}_i^T \ \mathbf{0}_{1 \times N}^T \right]^T$ and

$$\mathbf{D}_i = \begin{bmatrix} \mathbf{I}_{ML} \\ \mathbf{0}_{N \times ML} \end{bmatrix} \mathbf{C}_i \begin{bmatrix} \mathbf{0}_{N \times ML} & \mathbf{I}_N \end{bmatrix}. \quad (27)$$

The Riemannian gradient, $\text{grad} f(\mathbf{x}_i)$, at any given point \mathbf{x}_i is defined as the orthogonal projection of the Euclidean gradient $\nabla f(\mathbf{x}_i)$ onto the tangent space $T_{\mathbf{x}_i} \mathcal{M}$ of the manifold \mathcal{M} at point \mathbf{x}_i . This projection can be mathematically expressed

$$T_{\mathbf{x}_i} \mathcal{M} = \{ \mathbf{y} \in \mathbb{C}^{M+N_{\text{PR}}} \mid \text{Re}(\mathbf{y} \odot \mathbf{x}_i^*) = \mathbf{0}_{N_{\text{PR}}} \}. \quad (28)$$

Considering the objective function in hand, i.e. $f(\mathbf{x}) = \sum_{i=1}^{LM_t} |\mathbf{x}^H \bar{\mathbf{b}}_i + \mathbf{x}^H \mathbf{D}_i \mathbf{x}|^2$, the gradient in the Euclidean space at the point \mathbf{x} is expressed as

$$\nabla f(\mathbf{x}) = 2 \sum_{i=1}^{LM_t} \begin{bmatrix} (\mathbf{C}_i \phi + \mathbf{b}_i)(\phi^H \mathbf{C}_i^H \mathbf{w} + (\mathbf{w}^H \mathbf{b}_i)^*) \\ \mathbf{C}_i^H \mathbf{w} (\mathbf{w}^H \mathbf{C}_i \phi + \mathbf{w}^H \mathbf{b}_i) \end{bmatrix}, \quad (29)$$

where we have expressed the gradient in terms of \mathbf{w} and ϕ . Furthermore, the Riemannian gradient at \mathbf{x} is given as

$$\mathbf{g} = \text{grad} f(\mathbf{x}) = \nabla f(\mathbf{x}) - \text{Re}(\nabla f(\mathbf{x}) \odot \mathbf{x}^*) \odot \mathbf{x}. \quad (30)$$

Note that utilizing the Riemannian gradient allows extending optimization techniques from Euclidean space to manifold space. In addition, we would like to mention that the Armijo-Goldstein (or the backtracking line-search) is enforced as a first step of each iteration to ensure the monotonic decrease of $f(\mathbf{x})$ as \mathbf{x}_i is updated to \mathbf{x}_{i+1} . Moreover, the retraction step is defined as

$$\begin{aligned} \text{Retr}_{\mathbf{x}} : T_{\mathbf{x}} \mathcal{M} &\rightarrow \mathcal{M} \\ &: \alpha \mathbf{c} \rightarrow \text{Retr}_{\mathbf{x}}(\alpha \mathbf{c}), \end{aligned} \quad (31)$$

where $\text{Retr}_{\mathbf{x}}(\alpha \mathbf{c})$ is an $M \times 1$ vector given as

$$[\text{Retr}_{\mathbf{x}}(\alpha \mathbf{c})]_m = \frac{[\mathbf{x} + \alpha \mathbf{c}]_m}{\|[\mathbf{x} + \alpha \mathbf{c}]_m\|}. \quad (32)$$

Since \mathbf{c}_{i+1} and \mathbf{c}_i fall in different tangent spaces, hence the transport vector is introduced to map the previous search direction from its original tangent space to the current tangent space at the updated point \mathbf{x}_{i+1} . For this, we define the transport vector as

$$\begin{aligned} \mathcal{T}_{\mathbf{x}_i \rightarrow \mathbf{x}_{i+1}} : T_{\mathbf{x}_i} \mathcal{M} &\rightarrow T_{\mathbf{x}_{i+1}} \mathcal{M} \\ &: \mathbf{c} \rightarrow \mathbf{c} - \text{Re}(\mathbf{c} \odot \mathbf{x}_{i+1}^*) \odot \mathbf{x}_{i+1}. \end{aligned} \quad (33)$$

The RCG algorithm tailored to solve sub-problem (\mathcal{P}_1) in equation (23) is summarized in **Algorithm 1**. Referring to **Algorithm 1**, we can observe that the method operates of I iterations, which is an input parameter of the algorithm, and is related to the final obtained precision of the solution.

Next, given the current estimates of \mathbf{w} and ϕ , we can formulate a complementary sub-problem to solve for the

Algorithm 1 RCG-based optimization to solve (\mathcal{P}_1)

```

1: INPUT  $\{\mathbf{b}_i, \mathbf{C}_i\}_{i=1}^{LM_t}, I$ 
2: Initialize  $\mathbf{c}_0 = -\text{grad}(\mathbf{x}_0)$ .
3: Set  $i \leftarrow 0$ .
4: while  $i < I$  do
5:   Select step size  $\alpha_i$  based on backtracking line-search.
6:   Update  $\mathbf{x}_{i+1}$  via Retraction, i.e.  $\mathbf{x}_{i+1} = \text{Retr}_{\mathbf{x}_i}(\alpha_i \mathbf{c}_i)$ .
7:   Compute the Riemannian gradient  $\mathbf{g}_{i+1} = \text{grad} f(\mathbf{x}_{i+1})$  following (30)
8:   Compute transport vectors  $\mathbf{g}_i^+ = \mathcal{T}_{\mathbf{x}_i \rightarrow \mathbf{x}_{i+1}}(\mathbf{g}_i)$  in (33).
9:   Compute transport vectors  $\mathbf{c}_i^+ = \mathcal{T}_{\mathbf{x}_i \rightarrow \mathbf{x}_{i+1}}(\mathbf{c}_i)$  in (33).
10:  Update  $\beta_{i+1} = \frac{\|\mathbf{g}_{i+1}\|^2}{\|\mathbf{g}_i^+\|^2}$ 
11:  Update conjugate gradient as  $\mathbf{c}_{i+1} = -\mathbf{g}_{i+1} + \beta_{i+1} \mathbf{c}_{i+1}^+$ 
12:   $i \leftarrow i + 1$ 
13: end while
14: return  $\mathbf{x}_I = \begin{bmatrix} \mathbf{w}_I \\ \phi_I \end{bmatrix}$ 

```

statistical covariance matrix of the transmit symbols, which is the following

$$(\mathcal{P}_2) \begin{cases} \min_{\mathbf{R}_{ss}} P_{\text{PI}} \\ \text{s.t.} \quad \frac{\text{tr}(\mathbf{R}_{ss} \mathbf{H}_c^H(\phi) \mathbf{H}_c(\phi))}{M_r L \sigma_c^2} \geq \gamma_{\text{comm}}, \\ \frac{P_{\text{sense}}}{P_{\text{PI}} + P_{\text{obs}} + P_{\text{noise}}} \geq \gamma_{\text{sense}}, \\ \text{tr}(\mathbf{R}_{ss}) = P_B, \quad \mathbf{R}_{ss} \succeq \mathbf{0}. \end{cases} \quad (34)$$

With the help of equations, (16), (17), (18), and (19), the problem in (34) can be equivalently formulated in terms of traces as given at the bottom of the next page in equation (35). The equivalent problem in equation (35) is a convex optimization problem, and in particular an SDP problem, which is computationally tractable [74] and can be efficiently solved by off-the-shelf optimization software packages, such as MOSEK [75] or CVX [76]. The BCCD algorithm designed to solve problem (\mathcal{P}) in equation (21) is summarized in **Algorithm 2**. Referring to **Algorithm 2**, N_{iter} refers to the number of iterations of the main loop to be executed. Moreover, we have initialized $\mathbf{R}_{ss}^{(0)} = \mathbf{U}^H \mathbf{U}$, where \mathbf{U} is uniformly random matrix of size $LM_t \times LM_t$. This initialization was chosen to preserve the positive semi-definiteness of the covariance matrix $\mathbf{R}_{ss}^{(0)}$.

We would like to highlight that an interferers for communications and obstacles for sensing impact the performance in a crucial way. For communications, we can see that a higher level of average noise power at the user due to interference, i.e. σ_I^2 contributes to higher σ_c^2 , thus deteriorating the communication SNR in, i.e. $\frac{\text{tr}(\mathbf{R}_{ss} \mathbf{H}_c^H(\phi) \mathbf{H}_c(\phi))}{M_r L \sigma_c^2}$ appearing in the

$$(\mathcal{P}_2) \begin{cases} \min_{\mathbf{R}_{ss}} \text{tr}(\mathbf{A}_c^H(\phi) \mathbf{w} \mathbf{w}^H \mathbf{A}_c(\phi) \mathbf{R}_{ss}) \\ \text{s.t.} \quad \text{tr}(\mathbf{R}_{ss} \mathbf{H}_c^H(\phi) \mathbf{H}_c(\phi)) \geq \gamma_{\text{comm}} M_r L \sigma_c^2, \\ \text{tr}(\mathbf{A}_r^H(\phi) \mathbf{w} \mathbf{w}^H \mathbf{A}_r(\phi) \mathbf{R}_{ss} - \gamma_{\text{sense}} \sigma_r^2 \mathbf{w} \mathbf{w}^H - \gamma_{\text{sense}} \mathbf{A}_c^H(\phi) \mathbf{w} \mathbf{w}^H \mathbf{A}_c(\phi) \mathbf{R}_{ss} - \gamma_{\text{sense}} \mathbf{A}_o^H(\phi) \mathbf{w} \mathbf{w}^H \mathbf{A}_o(\phi) \mathbf{R}_{ss}) \geq 0, \\ \text{tr}(\mathbf{R}_{ss}) = P_B, \quad \mathbf{R}_{ss} \succeq \mathbf{0}. \end{cases} \quad (35)$$

constraints of (21). This means that more interference can lead to a less feasible γ_{comm} . For sensing, obstacles lead to a lower SNDR, hence impacting the possibility of targeting higher γ_{sense} . In fact, the added power from obstacles, P_{obs} , can be viewed as additional un-necessary power.

Algorithm 2 BCCD-based optimization to solve (\mathcal{P})

```

1: INPUT:  $\gamma_{\text{comm}}, \gamma_{\text{sense}}, \sigma_r^2, \sigma_c^2, I, N_{\text{iter}}, P_B$ 
2: Initialize  $\mathbf{R}_{ss}^{(0)}$ .
3: Set  $n \leftarrow 1$ .
4: while  $n < N_{\text{iter}}$  do
5:   Perform an eigenvalue decomposition (EVD) on  $\mathbf{R}_{ss}^{(n-1)}$ .
6:   Given  $\mathbf{R}_{ss}^{(n-1)}$ , compute  $\{\mathbf{b}_i, \mathbf{C}_i\}_{i=1}^{LM_t}$  following (24) and (25).
7:   Given  $\{\mathbf{b}_i, \mathbf{C}_i\}_{i=1}^{LM_t}$ , run Algorithm 1 to estimate  $\mathbf{w}^{(n)}$  and  $\phi^{(n)}$ .
8:   Given  $\mathbf{w}^{(n)}$  and  $\phi^{(n)}$ , solve  $(\mathcal{P}_2)$  in (35) to obtain  $\mathbf{R}_{ss}^{(n)}$ .
9:    $n \leftarrow n + 1$ 
10: end while
11: return  $\mathbf{w}, \mathbf{R}_{ss}, \phi$ 

```

*C. Computational Complexity**1) Complexity of the RCG-based optimization*

First, we analyze the computational complexity of Algorithm 1. Observe that we can decompose the complexity based on the associated updates, namely

$$T_{\text{Alg},1} = I (T_\alpha + T_{\mathbf{x}} + T_{\mathbf{g}} + T_{\mathbf{g}^+} + T_{\mathbf{c}^+} + T_\beta + T_{\mathbf{c}}), \quad (36)$$

where T_α is the computational complexity of selecting step size α_i through backtracking line-search, $T_{\mathbf{x}}$ is the complexity of the retraction step, and $T_{\mathbf{g}}, T_{\mathbf{g}^+}, T_{\mathbf{c}^+}, T_\beta, T_{\mathbf{c}}$ represent the complexities of updating $\mathbf{g}_{i+1}, \mathbf{g}_i^+, \mathbf{c}_i^+, \beta_{i+1}$, and \mathbf{c}_{i+1} , respectively. The backtracking line-search requires $\mathcal{O}(\log(1/\epsilon_1))$ iterations to generate a solution with accuracy $\epsilon_1 > 0$ [77], [78]. Moreover, each iteration involves computing the function f , which costs $\mathcal{O}(LM_t(ML + N)^2)$, which stems from the quadratic term, so, $T_\alpha = \mathcal{O}(LM_t(ML + N)^2 \log \frac{1}{\epsilon_1})$. The retraction step entails $LM + N$ divisions, hence a total cost of $T_{\mathbf{x}} = \mathcal{O}(LM + N)$. Updating \mathbf{g}_{i+1} necessitates the computation of $\nabla f(\mathbf{x})$ first. The major complexity involved in each summand term in (29) is due to $\mathbf{C}_i \phi$, which costs $\mathcal{O}(LMN)$ and $\mathbf{w}^H \mathbf{b}_i$ which requires $\mathcal{O}(LM)$. This means that the number of operations involved in computing $\nabla f(\mathbf{x})$ is $\mathcal{O}(LM_t(LMN + LM)) = \mathcal{O}(L^2 M_t MN)$. After computing the gradient $\nabla f(\mathbf{x})$, we notice that (30) involves two Hadamard operations of vectors of sizes $LM + N$, hence a complexity of $\mathcal{O}(LM + N)$. We conclude that $T_{\mathbf{g}} = \mathcal{O}(L^2 M_t MN)$ as $L^2 M_t MN \gg LM + N$ is the

dominating term. The number of flops to compute the transport vector \mathbf{g}_i^+ following (33) involves two Hadamard operations followed by a subtraction, which is $3(LM + N)$, therefore the order of complexity translates to $T_{\mathbf{g}^+} = \mathcal{O}(LM + N)$. Note that $T_{\mathbf{c}^+} = T_{\mathbf{g}^+}$, hence $T_{\mathbf{c}^+} = \mathcal{O}(LM + N)$. The update of β_i consists of two vector magnitude computations, $\|\mathbf{g}_i\|^2$ and $\|\mathbf{g}_{i+1}\|^2$, each of which cost $\mathcal{O}(LM + N)$. This is followed by a division operation which is $\mathcal{O}(1)$. We conclude that $T_\beta = \mathcal{O}(LM + N)$. Moreover, computing \mathbf{c}_{i+1} demands $LM + N$ additions and $LM + N$ multiplications, so $T_{\mathbf{c}} = \mathcal{O}(LM + N)$. Replacing all obtained complexities of $T_\alpha, T_x, T_g, T_{g^+}, T_{c^+}, T_\beta, T_c$ in (36) and by neglecting the non-dominating terms abiding by the definition of "big-oh", we conclude that the complexity of **Algorithm 1** is

$$T_{\text{Alg},1} = \mathcal{O}(LM_t(ML + N)^2 I \log(1/\epsilon_1) + L^2 M_t M N I). \quad (37)$$

Next, we conduct a complexity analysis on **Algorithm 2**.

2) Complexity of the BCCD-based optimization

Following the analysis of **Algorithm 1**, we now conduct a complexity analysis of **Algorithm 2**, which can be decomposed as

$$T_{\text{Alg},2} = N_{\text{iter}}(T_{\text{EVD}} + T_{\mathbf{b}} + T_{\mathbf{C}} + T_{\text{Alg},1} + T_{\mathcal{P}_2}), \quad (38)$$

where T_{EVD} is the cost to perform the EVD on $\mathbf{R}_{ss}^{(n-1)}$, $T_{\mathbf{b}}, T_{\mathbf{C}}$ are the costs of computing all $\{\mathbf{b}_i\}_{i=1}^{LM_t}$ and $\{\mathbf{C}_i\}_{i=1}^{LM_t}$, respectively. Moreover, $T_{\mathcal{P}_2}$ is the cost to solve (\mathcal{P}_2) . The complexity in decomposing $\mathbf{R}_{ss}^{(n-1)}$ via EVD is $T_{\text{EVD}} = \mathcal{O}(L^3 M_t^3)$. Each \mathbf{b}_i in (24) consists of a matrix multiplication of $\mathbf{I}_L \otimes \mathbf{H}_{\text{DPI}}$ with \mathbf{v}_i , which without any structure exploitation would yield $\mathcal{O}(L^2 M M_t)$, however, it should be pointed out that utilizing a peculiar structure of the Kronecker product in this case allows us to write

$$(\mathbf{I}_L \otimes \mathbf{H}_{\text{DPI}}) \mathbf{v}_i = \begin{bmatrix} \mathbf{H}_{\text{DPI}} \mathbf{v}_i^{(1)} \\ \vdots \\ \mathbf{H}_{\text{DPI}} \mathbf{v}_i^{(L)} \end{bmatrix}, \quad (39)$$

where $\mathbf{v}_i^{(\ell)}$ is defined below (25). Each operation of type $\mathbf{H}_{\text{DPI}} \mathbf{v}_i^{(\ell)}$ costs $\mathcal{O}(M M_t)$, hence by (39), the multiplication costs $\mathcal{O}(L M M_t)$ and we conclude that $T_{\mathbf{b}} = \mathcal{O}(L^2 M M_t^2)$. Each row of the matrix appearing in (25) consists of a multiplication $\mathbf{H}_{\text{CR}} \mathbf{v}_i^{(\ell)}$, which costs $\mathcal{O}(N M_t)$, $\forall \ell$. Moreover, $\mathbf{G}_{\text{r}}^H \text{diag}(\mathbf{H}_{\text{CR}} \mathbf{v}_i^{(\ell)})$ costs $\mathcal{O}(N M)$, due to the diagonal structure of the right multiplicand. Therefore, computing \mathbf{C}_i via (25) would necessitate $\mathcal{O}(L N M)$, hence $T_{\mathbf{C}} = \mathcal{O}(L^2 N M M_t)$. The complexity of solving (\mathcal{P}_2) in (35) depends on the integrated solver, but a common well-known approach in optimization theory to solve an SDP is via interior-point methods [77], e.g. *primal-dual path-following algorithm* [79]. With such an approach, and following [80], we have that

$$T_{\mathcal{P}_2} = \mathcal{O}\left(\max\{LM_t, 3\}^4 \sqrt{LM_t} \log(1/\epsilon_2)\right), \quad (40)$$

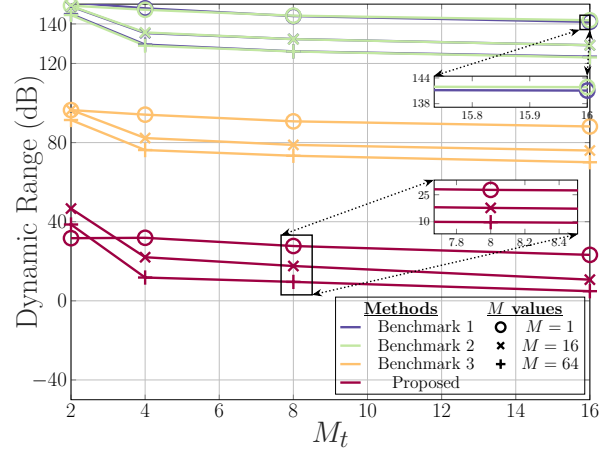


Fig. 3. Dynamic range behavior as a function of M_t . The number of samples is set to $L = 5$. The noise variances are set to $\sigma_c^2 = -80$ dBm and $\sigma_r^2 = -80$ dBm. The power budget is set to $P_B = 0$ dB. Also, $\gamma_{\text{comm}} = \gamma_{\text{sense}} = 0$ dB. The number of receiving antennas at the user is set to $M_r = 32$. The RIS size is $N_x = N_y = 32$.

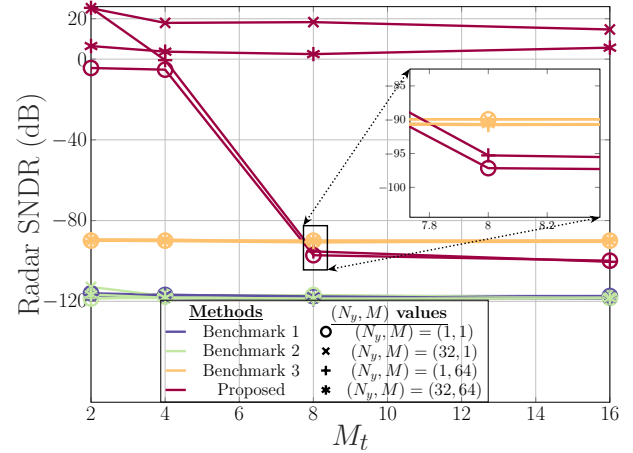


Fig. 4. The radar SNDR as a function of M_t for different RIS sizes and M . The values of $M_r, N_x, L, \sigma_c^2, \sigma_r^2, P_B, \gamma_{\text{comm}}, \gamma_{\text{sense}}$ are the same as those in Fig. 3.

where $\epsilon_2 > 0$ is the solution accuracy. Combining all the complexities, we get

$$\begin{aligned} T_{\text{Alg},2} = & \mathcal{O}\left(\max\{LM_t, 3\}^4 \sqrt{LM_t} N_{\text{iter}} \log(1/\epsilon_2)\right) \\ & + \mathcal{O}(LM_t(ML + N)^2 I N_{\text{iter}} \log(1/\epsilon_1)) + \\ & + \mathcal{O}((L^2 M_t M N I + L^2 N M M_t + L^2 M M_t^2) N_{\text{iter}}) \\ & + \mathcal{O}(L^3 M_t^3 N_{\text{iter}}). \end{aligned} \quad (41)$$

V. SIMULATION RESULTS

In this section, we present our simulation findings. Before we analyze and discuss our results, we mention the simulation parameters and benchmarks used in simulations.

A. Parameter Setup

Unless otherwise stated, we use the simulation parameters depicted in Table I. Monte Carlo type simulations is conducted in order to analyze the efficacy of the proposed method. In

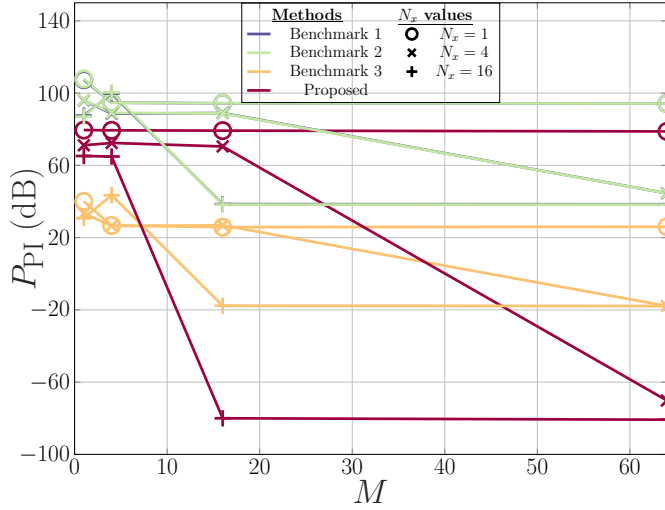


Fig. 5. The behavior of the PI power level as a function of M . The values of M_r , N_x , L , σ_c^2 , σ_r^2 , P_B , γ_{comm} , γ_{sense} are the same as those in Fig. 3. We fix $M_t = 32$, $M_r = 1$ and $N_y = 32$.

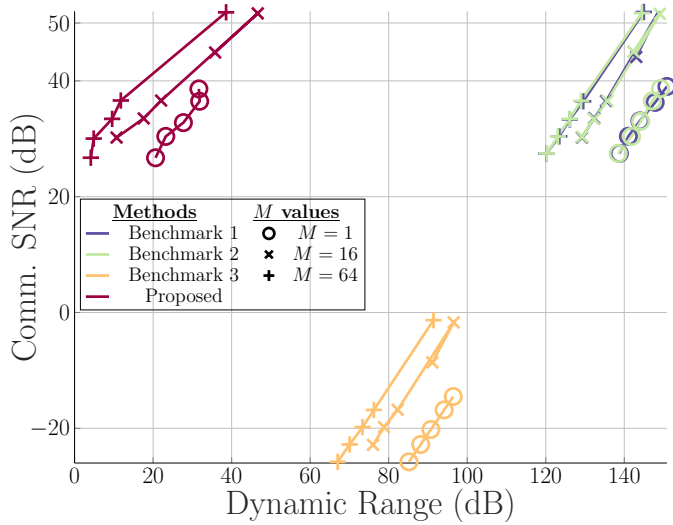


Fig. 6. The communication SNR versus the dynamic range for different values of M . The values of M_r , N_x , N_y , L , σ_c^2 , σ_r^2 , P_B , γ_{comm} , γ_{sense} are the same as those in Fig. 3.

typical radar applications [81], as well as communications [82], low noise amplifiers (LNAs) are specially designed to receive weak signals by boosting the incoming signal level. The cell radius is set to 500 meters [83]. Moreover, the carrier frequency is 28 GHz and the thermal noise is -174 dBm/Hz. Furthermore, the path-loss exponent is set to reflect a free space setting, i.e. 2. The antennas follow a uniform linear array (ULA) structure with spacing of half a wavelength, i.e. $\frac{\lambda}{2}$. At the PR, we have set the LNA gain to 40 dB gain, following [84] and the receive antenna gain at the PR is 25 dBi. At the RIS, we have set the reflecting RIS coefficient to unity, i.e. $A = 1$. Moreover, the single RIS element size is $d_x = d_y = 0.4\lambda$ [45]. At the BS, the transmit power is 40 dBm, and the transmit antenna gain is 25 dBi [85]. At the user, the receive antenna gain is 12 dBi [85]. The channel generated between nodes is Rayleigh. Also, we have set $Q = 0$.

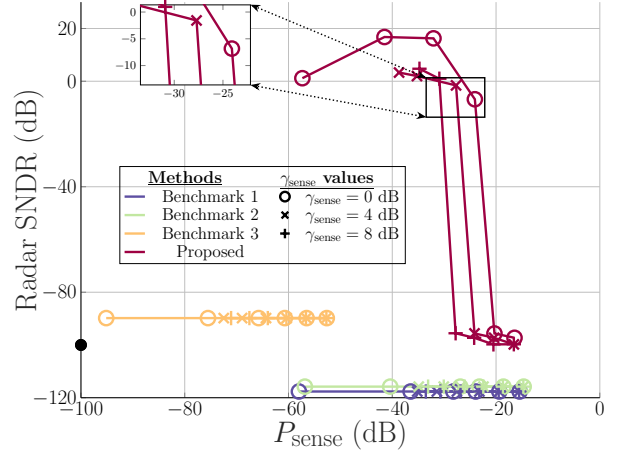


Fig. 7. The evolution of radar SNDR as a function of achievable sensing power. We set $M_t = 2$, $M_r = 1$, $N_x = N_y = 8$, $M = 24$, $L = 5$, $\sigma_c^2 = -100$ dBm, $\sigma_r^2 = -110$ dBm, and $\gamma_{\text{comm}} = 36$ dB.

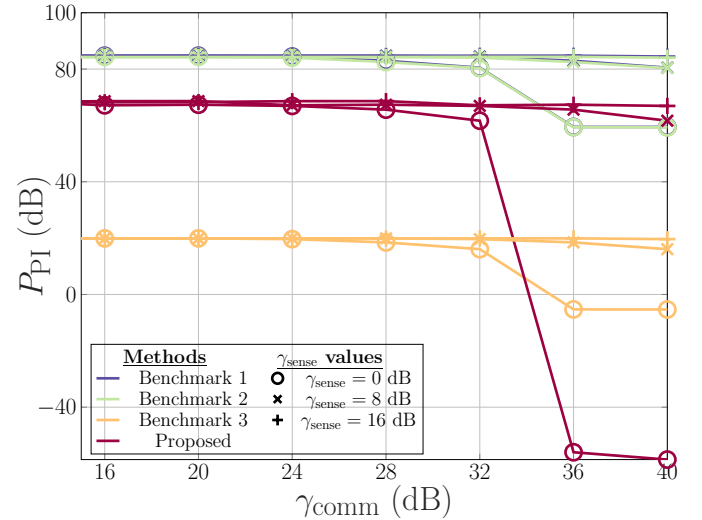


Fig. 8. The PI power level as a function of γ_{comm} . We set $P_B = 0$ dB. The values of M_t , M_r , N_x , N_y , M , L , σ_c^2 , and σ_r^2 are the same as those in Fig. 7.

TABLE I
SIMULATION PARAMETERS

Parameter	Value
Number of cells	1
Cell radius	500 m [83]
Carrier frequency (f_c)	28 GHz
Thermal noise	-174 dBm/Hz
Path-loss exponent	2 (free space)
Antenna spacing	$\frac{\lambda}{2}$
Reflecting RIS coefficient (A)	1
Single RIS element size (d_x, d_y)	0.4λ [45]
Transmit power by BS	40 dBm [85]
Transmit antenna gain at BS	25 dBi [85]
Receive antenna user gain	12 dBi [85]
Receive antenna PR gain	25 dBi [85]
LNA gain at PR	40 dB [84]
Antenna geometry	ULA
Channel conditions	Rayleigh [85]

B. Benchmark Schemes

Throughout simulations, we compare our proposed method with the following three schemes:

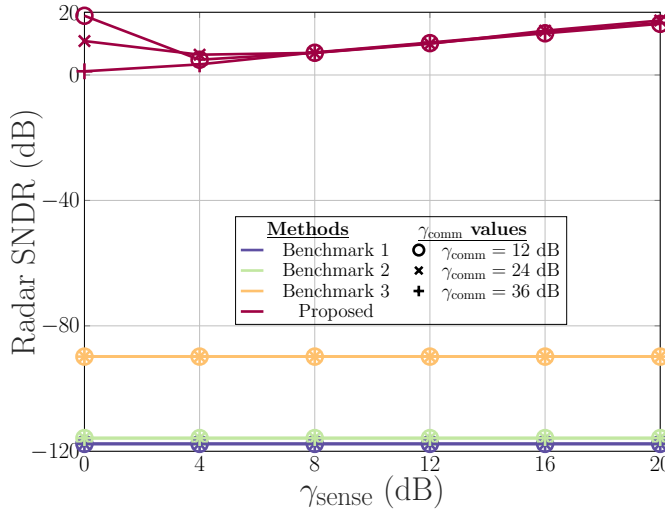


Fig. 9. The radar SNDR as a function of γ_{sense} . We set $\sigma_r^2 = -85$ dBm. The values of P_B , M_t , M_r , N_x , N_y , M , L , σ_c^2 are the same as those in Fig. 8.

- The random phase shift design where arbitrary values in the range $[0, 2\pi]$ are considered. In figure legends, this benchmark is denoted by **Benchmark 1**. Note that this benchmark is widely used within the RIS literature [86], [87], [88].
- The equal phase shift design where we fix the phase shifts of the RIS to be all equal to one another. In figure legends, this benchmark is denoted by **Benchmark 2**. Note that this benchmark is also common within the RIS [87], [89] and STAR-RIS [90] literature.
- This is a benchmark with no RIS deployment, and is denoted as **Benchmark 3** within the legends of the simulation figures. Only direct links are considered between BS-user, BS-target, BS-PR, and target-PR. Note that the no-RIS baseline is also a popular one within the RIS [91], [92], [93] literature. *A very important remark to highlight is the fact that RIS dimensions (N_x, N_y) appear on the legends of the no-RIS benchmark. This is due to the fact that the power consumed by our method is then passed to each other benchmark, including this one. Therefore, we have kept the RIS dimensions to have a fair assessment within simulations. In other words, all benchmarks operate at the same consumed power, i.e. $\text{tr}(\mathbf{R}_{ss})$.*

C. Simulation Results

a) Dynamic range behavior

In Fig. 3, we fix the number of receiving antennas at the user to $M_r = 32$. In addition, the RIS size is $N_x = N_y = 32$. The number of time samples is $L = 5$ samples, the communication noise variance was set to $\sigma_c^2 = -80$ dBm, the radar noise variance was fixed at $\sigma_r^2 = -80$ dBm. The power budget for the optimization method is $P_B = 0$ dB. In addition, we set $\gamma_{\text{comm}} = 0$ dB and $\gamma_{\text{sense}} = 0$ dB. We run the proposed method and average over Monte Carlo trials. The simulations reveal that increasing the number of transmit antennas, M_t can contribute to a decrease of the dynamic range at the PR for all benchmarks, as well as the proposed method. Generally

speaking, and in the high M_t regime, doubling the number of antennas decreases the dynamic range by roughly 5 dB. In addition, the number of antennas at the PR can aid in analog space-time beamforming to further lower down the dynamic range. For instance, at $M_t = 8$ antennas, the proposed method shows almost 10 dB reduction between when going from $M = 1$ to $M = 16$, in addition to another 10 dB reduction when increasing M from 16 to 64. Moreover, the proposed method can enormously reduce the dynamic range by factors of order of 50 dB as compared to a no-RIS setting (i.e. **Benchmark 3**). This can be explained by the accommodation of the PI within the optimization framework and accounting for its minimization rather than dealing with it in a separate stage. We also observe that **Benchmark 1** and **Benchmark 2** reveal similar performance.

b) Radar SNDR stability

In Fig. 4, we set the values of $M_r, N_x, L, \sigma_c^2, \sigma_r^2, P_B, \gamma_{\text{comm}}, \gamma_{\text{sense}}$ are the same as those in Fig. 3. This simulation shows that increasing the number of transmit antennas, M_t alone cannot guarantee a consistent radar SNDR, and increasing the RIS size can help overcome this issue through the proposed method. For example, when the number of RIS elements along the y-axis is set to only $N_y = 1$, then we can see that then radar SNDR drops after 8 BS antennas (for both $M = 1$ and $M = 64$ cases) to below the case of no-RIS indicating inefficient use of available power resources. Meanwhile, when $N_y = 32$ elements is used, the radar SNDR can be guaranteed to remain high. This is because more transmit antennas can contribute to deteriorate the radar SNDR by unwillingly injecting more PI into the model. The RIS can overcome this leakage and help maintain a high radar SNDR.

c) PI suppression

In Fig. 5, we set the values of $N_x, L, \sigma_c^2, \sigma_r^2, P_B, \gamma_{\text{comm}}, \gamma_{\text{sense}}$ are the same as those in Fig. 3. We also have $M_t = 32$ antennas, $M_r = 1$ antenna and $N_y = 32$. This simulation shows that the PR alone may not be fully helpful in maintaining a low PI power level. For instance, the PI power level with the proposed method remains around 80 dB for any $M \leq 64$ when $N_x = 1$. Upon increasing the RIS size to just $N_x = 4$, the PI power drops at $M = 64$ to a level beyond -60 dB, and, and at $M = 16$ for $N_x = 16$ also to a level beyond -60 dB. Also once can see that both benchmarks, **Benchmark 1** and **Benchmark 2** perform equally the same, and that the proposed method can bring the PI power level down beyond all the three benchmarks by 50 dB. This is because more RIS elements can provide extra degrees-of-freedom to aid the PR in its analog space-time beamforming task to further suppress the PI via the proposed optimization method.

d) Communication SNR & dynamic range tradeoff

In Fig. 6, we set the values of $M_r, N_x, N_y, L, \sigma_c^2, \sigma_r^2, P_B, \gamma_{\text{comm}}, \gamma_{\text{sense}}$ the same as those in Fig. 3. This simulation shows that the proposed method can achieve high communication SNR rates at a much lower dynamic range than the other benchmarking techniques. For example, if one targets a communication SNR of 30 dB, then the proposed method can achieve this communication

SNR with about 23 dB dynamic range with $M = 1$ antenna at the PR, whereby requiring more than 100 dB for both **Benchmark 1** and **Benchmark 2**. In addition, **Benchmark 3** can not achieve such a communication SNR of 30 dB due to the un-involvement of a RIS in that case. A counter-intuitive point to highlight is that increasing M can leave more room to enhance the communication SNR. Indeed, for a fixed dynamic range, increasing M can allow us to achieve a higher SNR. For example, a dynamic range of 20 dB can only achieve a 26 dB communication SNR with $M = 1$, whereas the same dynamic range can achieve an SNR of 35 dB for $M = 16$ and can even go beyond 40 dB for $M = 64$ antennas.

e) Radar SNDR behavior

In Fig. 7, we set $M_t = 2$ antennas, $M_r = 1$ antennas, $N_x = N_y = 8$ elements, $M = 24$ antennas and $L = 5$ samples. The value of σ_c^2 is fixed to -100 dBm and σ_r^2 is set to -110 dBm. In addition, we set $\gamma_{\text{comm}} = 36$ dB. This simulation studies the behavior of the radar SNDR as a function of achieved P_{sense} for different values of γ_{sense} . First, notice that the benchmarks reveal very low radar SNDR values, i.e. -90 dB for **Benchmark 3** (no-RIS) and an even lower radar SNDR for **Benchmark 1** and **Benchmark 2**, but a larger achieved P_{sense} due to the additional (however un-optimized) paths provided by the RIS. These low SNDR values are due to the dominating PI power level. To restore the radar SNDR to high values in order to achieve high target detection performance, our proposed method can reach SNDR values of -5 dB at ranges of P_{sense} within $[-32, -24]$ dB. In addition, for a fixed radar SNDR, γ_{sense} not only provides a clear control of radar SNDR, but also allows us to achieve SNDR targets for lower P_{sense} values. For example, to reach a radar SNDR value of -5 dB, one would require -24 dB of P_{sense} with a $\gamma_{\text{sense}} = 0$ dB, whereas a -28 dB for $\gamma_{\text{sense}} = 4$ dB and -32 dB for $\gamma_{\text{sense}} = 8$ dB. In essence, an increase of γ_{sense} allows for radar sensing operations to take place at lower sensing power.

f) Prioritizing Communications can help mitigate PI

In Fig. 8, we fix $P_B = 0$ dB. Moreover, the values of M_t , M_r , N_x , N_y , M , L , σ_c^2 , and σ_r^2 are the same as those in Fig. 7. This simulation studies the influence of γ_{comm} on the PI power level. We note that for all benchmarks, and the proposed method, when γ_{comm} dominates γ_{sense} (i.e. when communications is prioritized over sensing), the PI power level experiences an abrupt decrease, with the most significant drop observed in the proposed approach. For example, when $\gamma_{\text{comm}} = 40$ dB and $\gamma_{\text{sense}} = 0$ dB, the PI power level corresponding to the proposed method drops to below -40 dB, while remaining over 60 dB when $\gamma_{\text{sense}} \geq 8$ dB, which is still 15 dB lower than benchmarks 1 and 2. This means that communication tasks in the ISAC context can help in mitigating the PI power level.

g) Influence of γ_{sense} and γ_{comm} on radar SNDR

In Fig. 9, we fix $\sigma_r^2 = -85$ dBm. Moreover, the values of P_B , M_t , M_r , N_x , N_y , M , L , σ_c^2 , and the same as those in Fig. 8. This simulation studies the joint influence of γ_{sense} and γ_{comm} on the radar SNDR. First, we note that γ_{sense} controls the radar SNDR as expected. In particular, for the proposed method, the radar SNDR increases with γ_{sense} . In

addition, increasing γ_{comm} lowers the radar SNDR to settle at the boundary specified by γ_{sense} . Meanwhile, the radar SNDR levels of all benchmarks are always constant in this case and are below -80 dB.

VI. OPEN CHALLENGES

Developing a RIS-aided bi-static ISAC system presents challenges across multiple aspects. This paper proposes one technique for mitigating PI by directly suppressing it while satisfying relevant ISAC KPIs; nevertheless, alternative solutions tailored to different scenarios are also feasible. Implementing a bi-static ISAC system presents many open challenges, where we summarize a few below.

A. Near Field ISAC with PI mitigation

RISs have the potential to enable ISAC applications and in some cases enhance ISAC performance [94]. As far as PI mitigation is concerned, an open future challenge worth investigating is the potential to exploit wavefront curvature in geometric near-field conditions in order to further enhance communication SNR and radar SNDR, whilst maintaining a very low PI power level in near-field conditions. As the Fraunhofer distance is enlarged, the wavefronts within this region are spherical, which breaks the planar wavefront assumption. It is worth noting that RIS has already been explored for near-field sensing and beamforming [95] and localization [96], but remains un-explored in terms of PI mitigation for ISAC bi-static sensing. It is important to note that in near-field conditions, beamforming can concentrate signals around a specific location, namely *beamfocusing*, which has the full capacity of better improving the sensing and communications performance. Enabling this would entail redesigning the statistical transmit covariance and the space-time analog beamformers for improved PI mitigation.

B. Scaling up more RISs and PRs

While multiple RISs and PRs can provide additional spatial diversity, which can then enable the enhancement of the sensing performance, however more PIs will arise by construction of the model. This, in turn, opens an additional challenge and the need to jointly suppress the multiple PIs that arise. Another challenge that comes with scaling more RISs and PRs within the scene backhauling capacity connected with the CPU. In particular, if limited capacity backhaul links are installed, then a bottleneck can arise, hence bi-directional communication between the CPU and the PR, RIS and BS can be an additional challenge when incorporating additional RISs and PRs. This can include traffic to prioritize, in addition to the quantities to be exchanged, given throughput limitations. More specifically, once the CPU computes the statistical covariance matrix for the BS, along with the RIS phase shifts and the space-time beamformer, a fundamental question from backhauling perspective is, "Should the entire quantities be forwarded to the intended units, or should a compressed version of these quantities be sent?" Another question we can ask when scaling up PRs is that, "Can some of the processing be performed in a distributed manner? Said differently, can a distributed optimization algorithm be tailored to split the processing and

finally reducing traffic exchange to avoid possible bottlenecks?" This would require decomposing the formulated optimization problem in a distributed way requiring minimal input exchanges between the underlying subproblems.

C. ADC Optimization

An interesting line of research well-suited in this challenge is the few-bit (including 1-bit) ADC design. The goal is to design the ADC with smaller dynamic range that can accommodate signals with large power discrepancies [97], [98], [99]. For instance, the work in [100] proposes a generalized approximate message passing algorithm for low-resolution ADC that observed a 15 dB dynamic range reduction. An open challenge would be to design algorithms tailored for low-resolution (few-bit or/and 1-bit) ADCs to be able to extract the meaningful sensing data despite the presence of large PI power levels. To realize this, one common approach would be to introduce a b -bit quantization function, say $\mathcal{Q}_b(\cdot)$, to capture the quantization effects of the ADC. The received signal at the PR, and after analog beamforming, would be inputted to the ADC, i.e. $\mathcal{Q}_b(\mathbf{w}^H \mathbf{y}_t)$. The goal now would be to sense the target by observing $\mathcal{Q}_b(\mathbf{w}^H \mathbf{y}_t)$ instead of its continuous version, i.e. $\mathbf{w}^H \mathbf{y}_t$. Another approach would be to have an ADC per receive chain, which means that the PR would have to integrate M ADCs instead of just one, in the case of analog beamforming, which would add more PR processing complexity.

D. Imperfect channel state information

A more practical approach is to mitigate PI while carrying out ISAC tasks, even in the presence of imperfect CSI. The primary factors leading to imperfect CSI are inaccurate channel estimation and hardware imperfections [10]. In fact, ignoring these issues could significantly degrade overall system performance if they are not effectively addressed. To consider imperfect CSI, we may assume that the BS has access to CSI information in the form

$$\mathbf{H}_k = \widehat{\mathbf{H}}_k + \Delta \mathbf{H}_k, \quad (42)$$

where $\widehat{\mathbf{H}}_k$ is the estimated CSI and $\Delta \mathbf{H}_k$ stands for the CSI errors. A similar approach could be applied to the channels \mathbf{H}_{Rk} and \mathbf{H}_{cR} , as

$$\begin{aligned} \mathbf{H}_{cR} &= \widehat{\mathbf{H}}_{cR} + \Delta \mathbf{H}_{cR}, \\ \mathbf{H}_{Rk} &= \widehat{\mathbf{H}}_{Rk} + \Delta \mathbf{H}_{Rk}, \end{aligned} \quad (43)$$

where $\widehat{\mathbf{H}}_{cR}$, $\widehat{\mathbf{H}}_{Rk}$ represent the estimated CSI from BS to RIS and RIS to user, respectively. In addition, $\Delta \mathbf{H}_{cR}$, $\Delta \mathbf{H}_{Rk}$ represent their corresponding channel errors, respectively. Error modeling depends on whether a stochastic or deterministic approach is taken. In the former, the errors are usually assumed to be normally distributed. The latter, i.e. deterministic and norm bounded, corresponds to worst case optimization. One way to model this is to restrict the errors to live in a certain space, i.e. $\|\mathbf{E}_k^{\frac{1}{2}} \Delta \mathbf{H}_k\| \leq 1$, where \mathbf{E}_k controls the ellipsoidal shape of the CSI perturbation set for the direct channel. A similar restriction could be applied onto $\Delta \mathbf{H}_{Rk}$ and $\Delta \mathbf{H}_{cR}$. For sensing, we could also model the sensing channels, i.e.

the one-way, two-way, three-way and four-way channels, as done in (42), (43). An alternative, in case of strong LoS with the target, would be to assume uncertainty on some location information of the target itself, i.e. assume the target is at AoA θ_t from the PR and at angle of departure (AoD) ϕ_t from the BS, but the BS and target have partial knowledge of this. This means that the assumed channels would be $\widehat{\mathbf{g}}_t = \mathbf{a}_M(\widehat{\theta}_t)$, where $\widehat{\theta}_t \in [\theta_t - \frac{\Delta\theta}{2}; \theta_t + \frac{\Delta\theta}{2}]$ and $\widehat{\mathbf{h}}_t = \mathbf{a}_{M_t}(\widehat{\phi}_t)$, where $\widehat{\phi}_t \in [\phi_t - \frac{\Delta\phi}{2}; \phi_t + \frac{\Delta\phi}{2}]$. This modeling captures the case of any angle uncertainty on the location of the target. Indeed, the case of $\Delta\theta = \Delta\phi = 0$ corresponds to the case of perfect knowledge case. The same modeling could be applied onto the second, third and fourth order channels. The remaining challenge is to formulate a suitable optimization problem that can still be able to mitigate the PI while satisfying the minimal acceptable sensing and communication performance in the presence of all the CSI errors.

VII. CONCLUSION

This paper presented a novel framework for optimizing the dynamic range at a PR installed within a RIS-aided ISAC bistatic system. Due to RIS presence, additional interfering paths are present in the model, which we call PI. Moreover, we have introduced a dynamic range optimization approach that leverages space-time analog beamforming, in conjunction with RIS phase shift optimization to mitigate path interference PI, while maintaining both communication and sensing performance. The proposed BCCD algorithm effectively solves the resulting non-convex optimization problem, leading to significant improvements in system performance metrics such as SNDR and communication SNR. We have also analyzed the complexity of the proposed methods. This underscores the potential ISAC applications to exist with low dynamic range, particularly in the presence of multiple sensing reflectors.

APPENDIX A

PROBLEM EQUIVALENCE

For ease of representation, we first denote $\bar{\mathbf{H}}_{PI} = \bar{\mathbf{H}}_{DPI} + \bar{\mathbf{H}}_{RPI}$, where $\bar{\mathbf{H}}_{DPI} = \gamma_{DPI} \mathbf{H}_{DPI}$ and $\bar{\mathbf{H}}_{RPI} = \gamma_{RPI} \mathbf{H}_{RPI}$. To this end, we have the following series of steps

$$\begin{aligned} P_{PI} &= \mathbf{w}^H \mathbf{A}_c(\phi) \mathbf{R}_{ss} \mathbf{A}_c^H(\phi) \mathbf{w} \\ &\stackrel{(a)}{=} \sum_i \lambda_i |\mathbf{w}^H \mathbf{A}_c(\phi) \mathbf{v}_i|^2 \\ &\stackrel{(b)}{=} \sum_i \lambda_i |\mathbf{w}^H (\mathbf{I}_L \otimes \bar{\mathbf{H}}_{PI}) \mathbf{v}_i|^2 \\ &\stackrel{(c)}{=} \sum_i \lambda_i |\mathbf{w}^H (\mathbf{I}_L \otimes \bar{\mathbf{H}}_{DPI} + \mathbf{I}_L \otimes \bar{\mathbf{H}}_{RPI}) \mathbf{v}_i|^2 \\ &\stackrel{(d)}{=} \sum_i \lambda_i |\mathbf{w}^H (\mathbf{I}_L \otimes \bar{\mathbf{H}}_{DPI}) \mathbf{v}_i + \mathbf{w}^H (\mathbf{I}_L \otimes \bar{\mathbf{H}}_{RPI}) \mathbf{v}_i|^2 \\ &\stackrel{(e)}{=} \sum_i \lambda_i |\mathbf{w}^H (\mathbf{I}_L \otimes \bar{\mathbf{H}}_{DPI}) \mathbf{v}_i + \mathbf{w}^H (\mathbf{I}_L \otimes \mathbf{G}_{rR}^H \Phi \bar{\mathbf{H}}_{cR}) \mathbf{v}_i|^2 \\ &\stackrel{(f)}{=} \sum_i |\mathbf{w}^H \mathbf{b}_i + \mathbf{w}^H \mathbf{C}_i \phi|^2, \end{aligned}$$

where in step (a), we have decomposed \mathbf{R}_{ss} in terms of its eigenvalue decomposition, i.e. λ_i and \mathbf{v}_i represent the i^{th} eigenvalue and eigenvector of \mathbf{R}_{ss} , respectively. In step (b), we have used equation (10). In step (c), we have used equation (6). In step (d), we have distributed the inner-product. In step

(e), we have used equation (7). Finally, in step (f), we have used the diagonal commutative property, i.e. $\Phi \mathbf{a} = \text{diag}(\mathbf{a})\phi$, which holds true for any vector \mathbf{a} . The expressions of \mathbf{b}_i and \mathbf{C}_i are given in equations (24) and (25), respectively.

REFERENCES

- [1] M. Chafii, L. Bariah, S. Muhaidat, and M. Debbah, "Twelve scientific challenges for 6g: Rethinking the foundations of communications theory," *IEEE Communications Surveys & Tutorials*, vol. 25, no. 2, pp. 868–904, 2023.
- [2] W. Saad, M. Bennis, and M. Chen, "A vision of 6G wireless systems: Applications, trends, technologies, and open research problems," *IEEE network*, vol. 34, no. 3, pp. 134–142, 2019.
- [3] J. A. Zhang, M. L. Rahman, K. Wu, X. Huang, Y. J. Guo, S. Chen, and J. Yuan, "Enabling Joint Communication and Radar Sensing in Mobile Networks—A Survey," *IEEE Communications Surveys & Tutorials*, vol. 24, no. 1, pp. 306–345, 2022.
- [4] X. Cheng, D. Duan, S. Gao, and L. Yang, "Integrated Sensing and Communications (ISAC) for Vehicular Communication Networks (VCN)," *IEEE Internet of Things Journal*, vol. 9, no. 23, pp. 23 441–23 451, 2022.
- [5] Y. Cui, F. Liu, X. Jing, and J. Mu, "Integrating sensing and communications for ubiquitous iot: Applications, trends, and challenges," *IEEE Network*, vol. 35, no. 5, pp. 158–167, 2021.
- [6] Z. Wang, Y. Liu, X. Mu, Z. Ding, and O. A. Dobre, "NOMA Empowered Integrated Sensing and Communication," *IEEE Communications Letters*, vol. 26, no. 3, pp. 677–681, 2022.
- [7] H. Zhang, H. Zhang, B. Di, M. D. Renzo, Z. Han, H. V. Poor, and L. Song, "Holographic Integrated Sensing and Communication," *IEEE Journal on Selected Areas in Communications*, vol. 40, no. 7, pp. 2114–2130, 2022.
- [8] A. Bazzi and M. Chafii, "On Integrated Sensing and Communication Waveforms with Tunable PAPR," *IEEE Transactions on Wireless Communications*, pp. 1–1, 2023.
- [9] A. Bazzi and M. Chafii, "Secure Full Duplex Integrated Sensing and Communications," *IEEE Transactions on Information Forensics and Security*, vol. 19, pp. 2082–2097, 2024.
- [10] A. Bazzi and M. Chafii, "On Outage-based Beamforming Design for Dual-Functional Radar-Communication 6G Systems," *IEEE Transactions on Wireless Communications*, pp. 1–1, 2023.
- [11] S. Sun, F. Yang, J. Song, and R. Zhang, "Intelligent Reflecting Surface for MIMO VLC: Joint Design of Surface Configuration and Transceiver Signal Processing," *IEEE Transactions on Wireless Communications*, vol. 22, no. 9, pp. 5785–5799, 2023.
- [12] J. Chen, Y.-C. Liang, H. V. Cheng, and W. Yu, "Channel Estimation for Reconfigurable Intelligent Surface Aided Multi-User mmWave MIMO Systems," *IEEE Transactions on Wireless Communications*, vol. 22, no. 10, pp. 6853–6869, 2023.
- [13] M. Hua, Q. Wu, W. Chen, O. A. Dobre, and A. Lee Swindlehurst, "Secure Intelligent Reflecting Surface Aided Integrated Sensing and Communication," *IEEE Transactions on Wireless Communications*, pp. 1–1, 2023.
- [14] Z. Zhu, Z. Li, Z. Chu, Q. Wu, J. Liang, Y. Xiao, P. Liu, and I. Lee, "Intelligent Reflecting Surface-Assisted Wireless Powered Heterogeneous Networks," *IEEE Transactions on Wireless Communications*, pp. 1–1, 2023.
- [15] M. Nerini, S. Shen, and B. Clerckx, "Closed-Form Global Optimization of Beyond Diagonal Reconfigurable Intelligent Surfaces," *IEEE Transactions on Wireless Communications*, pp. 1–1, 2023.
- [16] M. D. Renzo *et al.*, "Smart radio environments empowered by reconfigurable AI meta-surfaces: An idea whose time has come," *EURASIP Journal on Wireless Communications and Networking*, vol. 2019, no. 1, pp. 1–20, 2019.
- [17] Y. Han, S. Jin, C.-K. Wen, and T. Q. Quek, "Localization and Channel Reconstruction for Extra Large RIS-Assisted Massive MIMO Systems," *IEEE Journal of Selected Topics in Signal Processing*, 2022.
- [18] S. Lin *et al.*, "Reconfigurable intelligent surfaces with reflection pattern modulation: Beamforming design and performance analysis," *IEEE Transactions on Wireless Communications*, vol. 20, no. 2, pp. 741–754, 2020.
- [19] W. Xu, J. Zhang, S. Cai, J. Wang, and Y. Wu, "RIS-assisted MIMO secure communications with Bob's statistical CSI and without Eve's CSI," *Digital Communications and Networks*, 2022.
- [20] G. Zhou, C. Pan, H. Ren, P. Popovski, and A. L. Swindlehurst, "Channel estimation for RIS-aided multiuser millimeter-wave systems," *IEEE Transactions on Signal Processing*, vol. 70, pp. 1478–1492, 2022.
- [21] C. Huang, A. Zappone, G. C. Alexandropoulos, M. Debbah, and C. Yuen, "Reconfigurable intelligent surfaces for energy efficiency in wireless communication," *IEEE Transactions on Wireless Communications*, vol. 18, no. 8, pp. 4157–4170, 2019.
- [22] C. Liaskos, A. Tsioliaridou, A. Pitsillides, S. Ioannidis, and I. Akyildiz, "Using any surface to realize a new paradigm for wireless communications," *Communications of the ACM*, vol. 61, no. 11, pp. 30–33, 2018.
- [23] B. Dawidowicz, P. Samczynski, M. Malanowski, J. Misiurewicz, and K. Kulpa, "Detection of moving targets with multichannel airborne passive radar," *IEEE Aerospace and Electronic Systems Magazine*, vol. 27, no. 11, pp. 42–49, 2012.
- [24] E. C. Strinati, G. C. Alexandropoulos, V. Sciancalepore, M. Di Renzo, H. Wymeersch, D.-T. Phan-Huy, M. Crozzoli, R. d'Errico, E. De Carvalho, P. Popovski *et al.*, "Wireless environment as a service enabled by reconfigurable intelligent surfaces: The RISE-6G perspective," in *2021 Joint European Conference on Networks and Communications & 6G Summit (EuCNC/6G Summit)*. IEEE, 2021, pp. 562–567.
- [25] Y. Liu *et al.*, "Reconfigurable Intelligent Surfaces: Principles and Opportunities," *IEEE Communications Surveys & Tutorials*, vol. 23, no. 3, pp. 1546–1577, 2021.
- [26] Q. Wu, B. Zheng, C. You, L. Zhu, K. Shen, X. Shao, W. Mei, B. Di, H. Zhang, E. Basar, L. Song, M. D. Renzo, Z.-Q. Luo, and R. Zhang, "Intelligent Surfaces Empowered Wireless Network: Recent Advances and the Road to 6G," *Proceedings of the IEEE*, pp. 1–40, 2024.
- [27] J. Ye, L. Huang, Z. Chen, P. Zhang, and M. Rihan, "Unsupervised Learning for Joint Beamforming Design in RIS-Aided ISAC Systems," *IEEE Wireless Communications Letters*, pp. 1–1, 2024, cited by: 0; All Open Access, Green Open Access.
- [28] R. S. P. Sankar, S. P. Chepuri, and Y. C. Eldar, "Beamforming in Integrated Sensing and Communication Systems with Reconfigurable Intelligent Surfaces," *IEEE Transactions on Wireless Communications*, vol. 23, no. 5, pp. 4017 – 4031, 2024.
- [29] R. Liu, M. Li, Q. Liu, and A. L. Swindlehurst, "SNR/CRB-Constrained Joint Beamforming and Reflection Designs for RIS-ISAC Systems," *IEEE Transactions on Wireless Communications*, pp. 1–1, 2023.
- [30] K. Chen, C. Qi, O. A. Dobre, and G. Y. Li, "Simultaneous Beam Training and Target Sensing in ISAC Systems with RIS," *IEEE Transactions on Wireless Communications*, vol. 23, no. 4, pp. 2696 – 2710, 2024, cited by: 2; All Open Access, Green Open Access.
- [31] D. Wang, A. Bazzi, and M. Chafii, "RIS-Enabled Integrated Sensing and Communication for 6G Systems," in *2024 IEEE Wireless Communications and Networking Conference (WCNC)*, 2024, pp. 1–6.
- [32] Y. Xu, Y. Li, J. A. Zhang, M. D. Renzo, and T. Q. S. Quek, "Joint Beamforming for RIS-Assisted Integrated Sensing and Communication Systems," *IEEE Transactions on Communications*, vol. 72, no. 4, pp. 2232 – 2246, 2024.
- [33] Y. He, Y. Cai, H. Mao, and G. Yu, "RIS-Assisted Communication Radar Coexistence: Joint Beamforming Design and Analysis," *IEEE Journal on Selected Areas in Communications*, vol. 40, no. 7, pp. 2131 – 2145, 2022.
- [34] W. Wei, X. Pang, C. Xing, N. Zhao, and D. Niyato, "STAR-RIS Aided Secure NOMA Integrated Sensing and Communication," *IEEE Transactions on Wireless Communications*, pp. 1–1, 2024, cited by: 0.
- [35] X. Mu, Y. Liu, L. Guo, J. Lin, and R. Schober, "Simultaneously Transmitting and Reflecting (STAR) RIS Aided Wireless Communications," *IEEE Transactions on Wireless Communications*, vol. 21, no. 5, pp. 3083–3098, 2022.
- [36] M. Li, S. Zhang, Y. Ge, Z. Li, F. Gao, and P. Fan, "STAR-RIS Aided Integrated Sensing and Communication over High Mobility Scenario," *IEEE Transactions on Communications*, pp. 1–1, 2024, cited by: 0; All Open Access, Green Open Access.
- [37] P. Wang, X. Zhou, Y. Fang, H. Zeng, and J. Chen, "GNSS-Based Passive Inverse SAR Imaging," *IEEE Journal of Selected Topics in Applied Earth Observations and Remote Sensing*, vol. 16, pp. 508–521, 2023.
- [38] K. Jedrzejewski, M. Malanowski, K. Kulpa, and M. Pożoga, "Experimental verification of passive radar space object detection with a single low-frequency array radio telescope," *IET Radar, Sonar & Navigation*, vol. 18, no. 1, pp. 68–77, 2024.
- [39] B. Debaillie, D.-J. van den Broek, C. Lavín, B. van Liempd, E. A. M. Klumperink, C. Palacios, J. Craninckx, B. Nauta, and A. Pärssinen, "Analog/RF Solutions Enabling Compact Full-Duplex Radios," *IEEE Journal on Selected Areas in Communications*, vol. 32, no. 9, pp. 1662–1673, 2014.
- [40] A. Sabharwal, P. Schniter, D. Guo, D. W. Bliss, S. Rangarajan, and R. Wichman, "In-Band Full-Duplex Wireless: Challenges and

- Opportunities,” *IEEE Journal on Selected Areas in Communications*, vol. 32, no. 9, pp. 1637–1652, 2014.
- [41] T. Peto, L. Dudas, and R. Seller, “Analog direct path interference suppression for FM based passive radars,” in *2018 28th International Conference Radioelektronika (RADIOELEKTRONIKA)*, 2018, pp. 1–6.
- [42] J. L. Garry, G. E. Smith, and C. J. Baker, “Direct signal suppression schemes for passive radar,” in *2015 Signal Processing Symposium (SPSymo)*, 2015, pp. 1–5.
- [43] A. Goldsmith, *Wireless Communications*. Cambridge university press, 2005.
- [44] A. Chowdary, A. Bazzi, and M. Chafii, “On Hybrid Radar Fusion for Integrated Sensing and Communication,” *IEEE Transactions on Wireless Communications*, pp. 1–1, 2024.
- [45] Y. Huang, J. Yang, W. Tang, C.-K. Wen, S. Xia, and S. Jin, “Joint Localization and Environment Sensing by Harnessing NLOS Components in RIS-Aided mmWave Communication Systems,” *IEEE Transactions on Wireless Communications*, vol. 22, no. 12, pp. 8797–8813, 2023.
- [46] N. V. Shende, O. Gürbüz, and E. Erkip, “Half-Duplex or Full-Duplex Communications: Degrees of Freedom Analysis Under Self-Interference,” *IEEE Transactions on Wireless Communications*, vol. 17, no. 2, pp. 1081–1093, 2018.
- [47] I. Shomorony and A. S. Avestimehr, “Worst-Case Additive Noise in Wireless Networks,” *IEEE Transactions on Information Theory*, vol. 59, no. 6, pp. 3833–3847, 2013.
- [48] S. P. Chepuri, N. Shlezinger, F. Liu, G. C. Alexandropoulos, S. Buzzi, and Y. C. Eldar, “Integrated Sensing and Communications With Reconfigurable Intelligent Surfaces: From signal modeling to processing,” *IEEE Signal Processing Magazine*, vol. 40, no. 6, pp. 41–62, 2023.
- [49] S. Buzzi, E. Grossi, M. Lops, and L. Venturino, “Foundations of MIMO Radar Detection Aided by Reconfigurable Intelligent Surfaces,” *IEEE Transactions on Signal Processing*, vol. 70, pp. 1749–1763, 2022.
- [50] J. Yin, C. Unal, M. Schleiss, and H. Russchenberg, “Radar Target and Moving Clutter Separation Based on the Low-Rank Matrix Optimization,” *IEEE Transactions on Geoscience and Remote Sensing*, vol. 56, no. 8, pp. 4765–4780, 2018.
- [51] M. Delamou, A. Bazzi, M. Chafii, and E. M. Amhoud, “Deep Learning-based Estimation for Multitarget Radar Detection,” in *2023 IEEE 97th Vehicular Technology Conference (VTC2023-Spring)*, 2023, pp. 1–5.
- [52] S. K. Sharma, E. Lagunas, S. Chatzinotas, and B. Ottersten, “Application of Compressive Sensing in Cognitive Radio Communications: A Survey,” *IEEE Communications Surveys & Tutorials*, vol. 18, no. 3, pp. 1838–1860, 2016.
- [53] J. L. Garry, C. J. Baker, and G. E. Smith, “Evaluation of Direct Signal Suppression for Passive Radar,” *IEEE Transactions on Geoscience and Remote Sensing*, vol. 55, no. 7, pp. 3786–3799, 2017.
- [54] H. Griffiths and C. Baker, “Passive coherent location radar systems. Part 1: Performance prediction,” *IEE Proceedings-Radar, Sonar and Navigation*, vol. 152, no. 3, pp. 153–159, 2005.
- [55] M. Malanowski, *Signal processing for passive bistatic radar*. Artech House, 2019.
- [56] I. Leyva-Mayorga, B. Soret, and P. Popovski, “Inter-Plane Inter-Satellite Connectivity in Dense LEO Constellations,” *IEEE Transactions on Wireless Communications*, vol. 20, no. 6, pp. 3430–3443, 2021.
- [57] L. Grannemann, A. Ichkov, P. Mähönen, and L. Simić, “Urban Outdoor Measurement Study of Phased Antenna Array Impact on Millimeter-Wave Link Opportunities and Beam Misalignment,” *IEEE Transactions on Wireless Communications*, vol. 20, no. 3, pp. 1727–1741, 2021.
- [58] C. Morgenstern, A. R. Chiriyath, A. Dutta, A. Herschfelt, Y. Rong, A. C. Molnar, A. B. Apsel, D. G. Landon, and D. W. Bliss, “Analog Self-Interference Mitigation for IBFD, Joint Radar-Communications in Vehicular Applications,” in *2022 IEEE Radar Conference (Radar-Conf22)*, 2022, pp. 1–6.
- [59] F. J. Soriano-Irigaray, J. S. Fernandez-Prat, F. J. Lopez-Martinez, E. Martos-Naya, O. Cobos-Morales, and J. T. Entrambasaguas, “Adaptive Self-Interference Cancellation for Full Duplex Radio: Analytical Model and Experimental Validation,” *IEEE Access*, vol. 6, pp. 65 018–65 026, 2018.
- [60] M. Trinkle and J. Li, “Zero-IF receivers for phased array radars,” in *2008 International Conference on Radar*, 2008, pp. 349–354.
- [61] A. Sheikholeslami, D. Goeckel, and H. Pishro-Nik, “Jamming Based on an Ephemeral Key to Obtain Everlasting Security in Wireless Environments,” *IEEE Transactions on Wireless Communications*, vol. 14, no. 11, pp. 6072–6081, 2015.
- [62] J. M. de la Rosa, “Sigma-Delta Modulators: Tutorial Overview, Design Guide, and State-of-the-Art Survey,” *IEEE Transactions on Circuits and Systems I: Regular Papers*, vol. 58, no. 1, pp. 1–21, 2011.
- [63] R. J. Van de Plassche, *CMOS integrated analog-to-digital and digital-to-analog converters*. Springer Science & Business Media, 2013, vol. 742.
- [64] P. Aziz, H. Sorensen, and J. van der Spiegel, “An overview of sigma-delta converters,” *IEEE Signal Processing Magazine*, vol. 13, no. 1, pp. 61–84, 1996.
- [65] C. Morgan and A. Healey, “A Comparison of 25 Gbps NRZ & PAM-4 Modulation Used in Reference, Legacy, & Premium Backplane Channels,” in *International Symposium on Microelectronics*, vol. 2012, no. 1. International Microelectronics Assembly and Packaging Society, 2012, pp. 000 283–000 294.
- [66] D. S. AD9683, “14-Bit, 170 MSPS/250 MSPS, JESD204B, Analog-to-Digital Converter.”
- [67] L. Jacques, J. N. Laska, P. T. Boufounos, and R. G. Baraniuk, “Robust 1-Bit Compressive Sensing via Binary Stable Embeddings of Sparse Vectors,” *IEEE Transactions on Information Theory*, vol. 59, no. 4, pp. 2082–2102, 2013.
- [68] R. Walden, “Analog-to-digital converter survey and analysis,” *IEEE Journal on Selected Areas in Communications*, vol. 17, no. 4, pp. 539–550, 1999.
- [69] C. Stöckle, J. Munir, A. Mezghani, and J. A. Nossek, “1-bit direction of arrival estimation based on Compressed Sensing,” in *2015 IEEE 16th International Workshop on Signal Processing Advances in Wireless Communications (SPAWC)*, 2015, pp. 246–250.
- [70] A. Swindlehurst, A. Saxena, A. Mezghani, and I. Fijalkow, “Minimum probability-of-error perturbation precoding for the one-bit massive MIMO downlink,” in *2017 IEEE International Conference on Acoustics, Speech and Signal Processing (ICASSP)*, 2017, pp. 6483–6487.
- [71] P. Kumari, S. A. Vorobyov, and R. W. Heath, “Adaptive Virtual Waveform Design for Millimeter-Wave Joint Communication–Radar,” *IEEE Transactions on Signal Processing*, vol. 68, pp. 715–730, 2020.
- [72] A. R. Chiriyath, S. Ragi, H. D. Mittelmann, and D. W. Bliss, “Novel Radar Waveform Optimization for a Cooperative Radar-Communications System,” *IEEE Transactions on Aerospace and Electronic Systems*, vol. 55, no. 3, pp. 1160–1173, 2019.
- [73] Q. Wang, C. Xing, C. Du, L. Zhao, and L. Hanzo, “Hybrid Nonlinear Transceiver Optimization for the RIS-Aided MIMO Downlink,” *IEEE Transactions on Communications*, vol. 70, no. 10, pp. 6441–6455, 2022.
- [74] B. Li, M. Zhang, Y. Rong, and Z. Han, “Transceiver Optimization for Wireless Powered Time-Division Duplex MU-MIMO Systems: Non-Robust and Robust Designs,” *IEEE Transactions on Wireless Communications*, vol. 21, no. 6, pp. 4594–4607, 2022.
- [75] E. D. Andersen and K. D. Andersen, “The MOSEK Interior Point Optimizer for Linear Programming: An Implementation of the Homogeneous Algorithm,” in *High performance optimization*. Springer, 2000, pp. 197–232.
- [76] M. Grant and S. Boyd, “CVX: MATLAB Software for Disciplined Convex Programming, version 2.1,” 2014.
- [77] S. P. Boyd and L. Vandenberghe, *Convex optimization*. Cambridge university press, 2004.
- [78] T. Feng, X. Gu, and B. Liang, “Random Caching Design for Multi-User Multi-Antenna HetNets With Interference Nulling,” *IEEE Transactions on Wireless Communications*, vol. 22, no. 12, pp. 8965–8982, 2023.
- [79] C. Helmberg, F. Rendl, R. J. Vanderbei, and H. Wolkowicz, “An Interior-Point Method for Semidefinite Programming,” *SIAM Journal on Optimization*, vol. 6, no. 2, pp. 342–361, 1996. [Online]. Available: <https://doi.org/10.1137/0806020>
- [80] Z.-q. Luo, W.-k. Ma, A. M.-c. So, Y. Ye, and S. Zhang, “Semidefinite Relaxation of Quadratic Optimization Problems,” *IEEE Signal Processing Magazine*, vol. 27, no. 3, pp. 20–34, 2010.
- [81] K. Raghunandan, *RADAR for a Better Society*. Cham: Springer International Publishing, 2022, pp. 379–404. [Online]. Available: https://doi.org/10.1007/978-3-030-92188-0_18
- [82] Z. Liu, C.-H. Lee, W. Xu, and S. Li, “Energy-Efficient Design for Massive MIMO With Hardware Impairments,” *IEEE Transactions on Wireless Communications*, vol. 20, no. 2, pp. 843–857, 2021.
- [83] B. Ma, H. Shah-Mansouri, and V. W. S. Wong, “Full-Duplex Relaying for D2D Communication in Millimeter Wave-based 5G Networks,” *IEEE Transactions on Wireless Communications*, vol. 17, no. 7, pp. 4417–4431, 2018.
- [84] L. G. da Silva, L. C. Alexandre, P. Xiao, and A. C. S., “RIS Development and Implementation in a mm-Waves 5G-NR System Towards 6G,” *IEEE Wireless Communications Letters*, pp. 1–1, 2023.
- [85] I. A. Hemadeh, K. Satyanarayana, M. El-Hajjar, and L. Hanzo, “Millimeter-Wave Communications: Physical Channel Models, Design

- Considerations, Antenna Constructions, and Link-Budget,” *IEEE Communications Surveys & Tutorials*, vol. 20, no. 2, pp. 870–913, 2018.
- [86] C. You, B. Zheng, and R. Zhang, “Channel Estimation and Passive Beamforming for Intelligent Reflecting Surface: Discrete Phase Shift and Progressive Refinement,” *IEEE Journal on Selected Areas in Communications*, vol. 38, no. 11, pp. 2604–2620, 2020.
- [87] T. Van Chien, L.-T. Tu, W. Khalid, H. Yu, S. Chatzinotas, and M. Di Renzo, “RIS-Assisted Wireless Communications: Long-Term Versus Short-Term Phase Shift Designs,” *IEEE Transactions on Communications*, vol. 72, no. 2, pp. 1175–1190, 2024.
- [88] J. An, C. Xu, L. Gan, and L. Hanzo, “Low-Complexity Channel Estimation and Passive Beamforming for RIS-Assisted MIMO Systems Relying on Discrete Phase Shifts,” *IEEE Transactions on Communications*, vol. 70, no. 2, pp. 1245–1260, 2022.
- [89] H. An Le, T. Van Chien, V. D. Nguyen, and W. Choi, “Double RIS-Assisted MIMO Systems Over Spatially Correlated Rician Fading Channels and Finite Scatterers,” *IEEE Transactions on Communications*, vol. 71, no. 8, pp. 4941–4956, 2023.
- [90] A. Papazafeiropoulos, H. Q. Ngo, P. Kourtessis, and S. Chatzinotas, “STAR-RIS Assisted Cell-Free Massive MIMO System Under Spatially-Correlated Channels,” *IEEE Transactions on Vehicular Technology*, pp. 1–16, 2023.
- [91] W. Wang, W. Ni, H. Tian, Y. C. Eldar, and R. Zhang, “Multi-Functional Reconfigurable Intelligent Surface: System Modeling and Performance Optimization,” *IEEE Transactions on Wireless Communications*, pp. 1–1, 2023.
- [92] J. Yaswanth, M. Katwe, K. Singh, S. Prakriya, and C. Pan, “Robust Beamforming Design for Active-RIS Aided MIMO SWIPT Communication System: A Power Minimization Approach,” *IEEE Transactions on Wireless Communications*, pp. 1–1, 2023.
- [93] B. Sihlbom, M. I. Poulakis, and M. Di Renzo, “Reconfigurable Intelligent Surfaces: Performance Assessment Through a System-Level Simulator,” *IEEE Wireless Communications*, vol. 30, no. 4, pp. 98–106, 2023.
- [94] R. P. Sankar, S. P. Chepuri, and Y. C. Eldar, “Beamforming in Integrated Sensing and Communication Systems with Reconfigurable Intelligent Surfaces,” *IEEE Transactions on Wireless Communications*, pp. 1–1, 2023.
- [95] Y. Jiang, F. Gao, M. Jian, S. Zhang, and W. Zhang, “Reconfigurable Intelligent Surface for Near Field Communications: Beamforming and Sensing,” *IEEE Transactions on Wireless Communications*, vol. 22, no. 5, pp. 3447–3459, 2023.
- [96] C. Ozturk, M. F. Keskin, H. Wymeersch, and S. Gezici, “RIS-Aided Near-Field Localization Under Phase-Dependent Amplitude Variations,” *IEEE Transactions on Wireless Communications*, vol. 22, no. 8, pp. 5550–5566, 2023.
- [97] N. J. Myers, A. Mezghani, and R. W. Heath, “Swift-Link: A Compressive Beam Alignment Algorithm for Practical mmWave Radios,” *IEEE Transactions on Signal Processing*, vol. 67, no. 4, pp. 1104–1119, 2019.
- [98] C.-Y. Wu, T. Zhang, J. Li, and T. F. Wong, “Parameter Estimation in PMCW MIMO Radar Systems With Few-Bit Quantized Observations,” *IEEE Transactions on Signal Processing*, vol. 70, pp. 810–821, 2022.
- [99] C. T. Rodenbeck, M. Martinez, J. B. Beun, J. Silva-Martinez, A. I. Karşilayan, and R. Liechty, “When Less Is More . . . Few Bit ADCs in RF Systems,” *IEEE Access*, vol. 7, pp. 12 035–12 046, 2019.
- [100] P. Kumari, A. Mezghani, and R. W. Heath, “A Low-Resolution ADC Proof-of-Concept Development for a Fully-Digital Millimeter-wave Joint Communication-Radar,” in *ICASSP 2020 - 2020 IEEE International Conference on Acoustics, Speech and Signal Processing (ICASSP)*, 2020, pp. 8619–8623.